Journal Pre-proof

Porous biochar for improving the CO_2 uptake capacities and kinetics of concrete

Matthieu Mesnage, Rachelle Omnée, Johan Colin, Hamidreza Ramezani, Jena Jeong, Encarnacion Raymundo-Piñero

PII: S0958-9465(25)00014-9

DOI: https://doi.org/10.1016/j.cemconcomp.2025.105932

Reference: CECO 105932

To appear in: *Cement and Concrete Composites*

Received Date: 11 December 2023

Revised Date: 30 October 2024

Accepted Date: 7 January 2025

Please cite this article as: M. Mesnage, R. Omnée, J. Colin, H. Ramezani, J. Jeong, E. Raymundo-Piñero, Porous biochar for improving the CO_2 uptake capacities and kinetics of concrete, *Cement and Concrete Composites*, https://doi.org/10.1016/j.cemconcomp.2025.105932.

Porous biochar for improving the CO_2 uptake capacities and kinetics of concrete

Matthieu Mesnage[1], Rachelle Omnée[1], Johan Colin[2], Hamidreza Ramezani[3], Jena Jeong[2*], Encarnacion Raymundo-Piñero[1*]

[1]*CNRS, CEMHTI UPR3079, Univ. Orléans, 1D avenue de la Recherche Scientifique, 45071, Orléans, France*

[2]*IRC (Institut de Recherche en Constructibilité), ESTP, 94230 Cachan, France*

[3]*ICMN (Interfaces, Confinement, Matériaux, Nanostructures), CNRS, Université d'Orléans, 45071 Orléans, France*

* Corresponding author

Encarnación RAYMUNDO-PIÑERO

CEMHTI-CNRS Orleans

Site Haute Température

1D avenue de la Recherche Scientifique

CS 90055 45071 Orléans cedex 2

France

raymundo@cnrs-orleans.fr

Keywords : CO_2 uptake; concrete; biochar; carbonation kinetics; porosity; CO_2 diffusivity

Abstract

Carbonation is a natural process in concrete where atmospheric CO_2 diffuses into the pores of the material and reacts with cement hydrates to form calcium carbonate. Although this process can help to sequester atmospheric CO_2 and mitigate rising levels in urban areas, it slows down over time, resulting in low CO_2 uptake over the service life of concrete. This study proposes a sustainable method to improve carbonation kinetics and CO_2 capture in cement materials by incorporating highly porous biochar. The biochar, derived from seaweed pyrolysis, has a highly developed surface area, including micropores optimised for CO_2 adsorption, mesopores and macropores, as well as oxygen-rich surface groups. These properties allow the biochar to efficiently adsorb CO_2 and retain water. The biochar particles embedded in the cement matrix act as reservoirs for water and CO_2, influencing hydration and carbonation. The addition of biochar increases water retention in the composite, which promotes the formation of capillary pores and enhances the carbonation process. Experimental data and numerical simulations show that the adsorption of CO_2 in the micropores of biochar facilitates the flow of CO_2 through the composite, allowing deeper carbonation. The interaction between biochar and cement matrix enhances CO_2 diffusion and promotes calcium carbonate formation both within the biochar and at the biochar-cement interface, further improving CO_2 uptake. The study demonstrates that the incorporation of porous biochar into cement materials significantly increases their potential for CO_2 capture, offering a promising approach to sustainable construction and carbon sequestration.

1. Introduction

Since the beginning of the 20th century, the expansion of industries worldwide, coupled with the proliferation of individual transportation powered by fossil fuels, has dramatically increased global CO_2 emissions [1]. Locally, these heightened anthropogenic CO_2 emissions contribute to rising atmospheric CO_2 concentrations. Currently, typical outdoor concentrations range between 400 and 500 ppm; however, in urban environments—such as underground parking lots or tunnels—concentrations frequently exceed 500 ppm and can reach up to 1000 ppm, depending on factors such as time, weather, and traffic density [2]. In indoor spaces, CO_2 concentrations can easily surpass 1000 ppm, raising concerns about health issues, particularly among vulnerable groups like young children [3–5]. Consequently, in addition to the ecological challenges posed by rising CO_2 emissions, there are significant health implications in indoor environments, as the efficiency of air ventilation is heavily reliant on the quality of outdoor air [6].

In parallel with efforts to reduce CO_2 emissions, capturing and storing CO_2 in urban areas could be effectively achieved using concrete materials. Indeed, concrete—the most widely used construction material—has a natural capacity to capture CO_2 within its intrinsic porosity and to store it through a natural carbonation process. Traditionally, carbonation of concrete has been viewed as a detrimental process that adversely affects the durability of reinforced concrete structures [7–10]. However, several studies have demonstrated through kinetic models that concrete possesses the potential for CO_2 storage throughout its life cycle [11–13]. Nonetheless, the carbonation process tends to slow over time. The primary driving force behind this phenomenon is the diffusion of CO_2 into the porous capillary network of concrete [14]. The CO_2 gas combines with the condensed water layer surrounding the pore walls [15] to form carbonate ions (CO_3^{2-}), releasing H^+ ions. These CO_3^{2-} ions and H^+ then react with cement hydrates, leading to the precipitation of calcium carbonate ($CaCO_3$) and the release of water [11,16]. Since $CaCO_3$ has a greater molar volume than hydrates [17,18], its precipitation results in progressive clogging of capillary pores, reducing pore diameters [15,17,19] and consequently lowering CO_2 diffusivity, which in turn adversely affects carbonation kinetics [15,20,21].

At the end of service life of concrete building, the material can be reused as Recycled Concrete Aggregate (RCA) following demolition. Recent findings indicate that RCA exhibits higher CO_2 uptake capacities due to its increased exposed surface area after crushing and grinding [22]. Research has shown that CO_2 capture in RCA can reach between 2% and 5% by weight. Additionally, the size of the RCA and its degree of water saturation significantly influence its carbonation. Although carbonated RCA demonstrates improved mechanical strength [23], its reuse in practical engineering applications remains limited due to the management and energy demands associated with CO_2 carbonation processes on an industrial scale.

Thus, the present study aims to address the limitations of CO_2 uptake capacity in concrete materials by developing composite materials that incorporate RCA alongside a new component: porous carbon with high CO_2 uptake capacities. Porous carbons are versatile materials characterized by high specific surface areas and nanometric pore dimensions, which can be tailored through the selection of precursor materials and synthesis methods. This highly developed porous structure, encompassing microporosity (diameter $\leq$ 2 nm), mesoporosity (2 nm $\leq$ diameter $\leq$ 50 nm), and macroporosity (diameter $\geq$ 50 nm), enables the adsorption of a wide range of gas molecules, including CO_2 [24]. The adsorption of gas molecules in the porosity of carbon is driven by the high internal energy of the carbon atoms at the pore surfaces, which facilitates the retention of gas adsorbate molecules via Van der Waals forces within the porous structure [25]. Additionally, the presence of surface functional groups, particularly heteroatoms like oxygen at the edges of the carbon graphene layers, enhances adsorption of polar adsorbate molecules such as water. While sedimentary rocks, including bituminous coal [26] and lignite [27], can be utilized, biomass waste currently represents the primary feedstock, allowing for the recycling of various low-cost carbonaceous organic materials on a large scale [28]. Furthermore, the production of carbon materials from waste biomass may yield a negative carbon footprint, as the CO_2 sequestered during the photosynthesis of biomass exceeds the emissions produced during synthesis [29,30]. Biochars are normally produced through the thermal treatment (pyrolysis) in an inert atmosphere of carbon-rich precursors. Biochar typically exhibits specific surface areas below 350 m^2 g^{-1} [31,32]. The production of porous carbons from a biochar requires an additional so-called activation process to increase porosity and CO_2 uptakes capacities [24,31].

In recent years, the incorporation of biomass-based carbon materials, such as biochar, as additives in cementitious materials has been proposed as a mitigation strategy to reduce CO_2 emissions while simultaneously enhancing certain mechanical or thermal properties. Substituting a portion of cement with a material that has a negative carbon footprint could contribute to reducing CO_2 emissions within the construction sector. Studies have demonstrated that incorporating biochar powders into concrete can enhance mechanical strength through filler effects and increased densification of the cement matrix during carbonation curing [32–40]. The porous characteristics of biochars also positively influence the thermal insulation properties of cement by enhancing thermal resistance [41]. However, the use of highly porous carbon materials to improve the CO_2 uptake capacity of concrete has been infrequently reported. Horgnies et al. have published several reports evaluating the beneficial effects of adding porous carbon to fresh concrete to increase NO_2 adsorption in the hardened product [42–44]. Nevertheless, no studies have specifically focused on enhancing concrete carbonation during its service life for atmospheric CO_2 removal through the incorporation of a high surface area biochar, due to the presence of a large amount of micropores with sizes ~0.65-0.8 nm adapted to CO_2 adsorption [24]. In this study, we propose such a highly porous biochar with a large volume of micropores, taking advantage of the fact that direct pyrolysis of seaweed biomass has been shown to be a promising

method for producing high surface area carbon without additional activation processes. Specifically, pyrolysis of seaweeds rich in carrageenan or sodium alginate has resulted in porous biochars with specific surface areas exceeding 1000 m^2/g [45].

Therefore, the purpose of this study is to develop a functional composite material with enhanced CO_2 storage capacities compared to conventional cementitious materials. The limitations of CO_2 uptake capacity in concrete will be addressed by formulating composite materials that incorporate both porous biochar and RCA. The CO_2 uptake capacity of these composite materials will be evaluated using a controlled CO_2 chamber, with regulated temperature and humidity over several days. The quantification of CO_2 uptake during carbonation will facilitate kinetic tracking to study the role of porous carbon in CO_2 capture. In addition to CO_2 quantification, physicochemical characterizations will be conducted at various carbonation intervals to gain deeper insights into the synergistic effects of biochar on concrete carbonation. To further investigate the influence of carbon particles on CO_2 uptake in the composite materials, numerical simulations modelling the passage of CO_2 through the cement matrix into the carbon porosity will also be performed.

2. Materials and methods

2.1. Materials manufacturing

2.1.1. Porous biochar

The biomass selected for the preparation of biochar (LN 750) was Lessonia Negrescens, a type of brown seaweed. The stems and leaves were cut into approximately 5–7 mm particles, and pyrolysis was conducted using a Carbolite Gero HST 12/200 horizontal split tube furnace at 750 °C for 3 hours, with a heating rate of 10 °C/min under an argon atmosphere to prevent oxidation. Following pyrolysis, the resulting biochar particles were washed with distilled water and dried at 100 °C. As previously mentioned, no activation steps were necessary to create a porous material, as self-activation occurred due to the chemical composition of the seaweed during thermal decomposition [45,46].

2.1.2. Composite materials

Composite materials, consisting of a cement matrix and recycled concrete aggregates (RCA) sourced from BONNA SABLA, France, were prepared according to two formulations. The first formulation served as a reference material without porous biochar (composite Type I), while the second included LN 750 biochar particles (composite Type II). Ordinary Portland cement (CEM I 52.5) was used as the matrix in both formulations. Type I contained only RCA, whereas Type II included both RCA and LN 750. The volume of biochar added was equivalent to the volume of RCA replaced, ensuring that the (aggregates + carbon)/cement volumetric ratio in Type II was equal to the aggregates/cement volumetric ratio in Type I. Both the RCA and biochar particles had a granulation size ranging from 5

to 7 mm. After mixing with a water/cement ratio of 0.45, the composite materials were cast in silicon molds measuring 7 x 3 x 2.5 cm^3. Nine molds were filled for each formulation and placed in a desiccator filled with water to maintain a moisture-saturated atmosphere (RH ≈ 100%). Hydration was allowed to continue for a minimum of 28 days.

2.2. Physico-chemical characterization of materials and composites

The characterization of porous texture of the biochar was conducted through gas adsorption using nitrogen at 77 K and carbon dioxide at 273 K with a Quadrasorb Evo Analyser. Nitrogen was utilized as the adsorbate to assess microporosity (0.7 nm <pore diameter<2 nm) and mesoporosity (2 nm <pore diameter<50 nm), while carbon dioxide was employed to evaluate small microporosity (i.e., pore diameter < 0.7 nm). Specific surface areas were calculated from the nitrogen adsorption isotherm using the Brunauer-Emmett-Teller (BET) model, and pore size distributions were determined using Non-Local Density Functional Theory (NLDFT). Adsorption isotherms for carbon dioxide gas were measured at 273 K (0 °C) and 298 K (25 °C). The specific surface area and volume of the micropores were calculated by applying the Dubinin-Radushkevich (DR) model to the carbon dioxide adsorption isotherm at 273 K. The carbon dioxide adsorption capacity of LN 750 biochar at room temperature was determined by performing a carbon dioxide adsorption isotherm at 298 K.

Characterization of the large mesopore and macropore ranges was performed on both the materials and composites using Mercury Intrusion Porosimetry (MIP) with a Micromeritics Autopore IV porosimeter. The contact angle (θ) was set to 130°, and the mercury surface tension (γ) was set to 485 mN/m. Applied pressures ranging from 1.46 kPa to 206.8 MPa enabled the assessment of pore sizes from 6 nm to 854 µm, using the Washburn equation [47]. For LN 750, samples were first dried in an oven at 100 °C for 24 hours to remove any moisture. In contrast, composite materials and RCA samples were dried at a maximum of 70 °C for 24 hours to avoid the removal of bound water contained within the cement hydrates.

Open porosity, density, and water sorption were determined using hydrostatic weighing, applied to the composite materials, LN 750, and RCA. After drying the samples, air was evacuated from the pores under vacuum. Subsequently, the out-gassed materials were immersed in water to monitor water uptake. Open porosity, bulk and skeletal densities, and the water sorption coefficient were calculated from the scaled masses according to the following equations:

$$\Phi = \frac{m_h - m_s}{m_h - m_i} \times 100 \quad (1)$$

$$\rho_b = \frac{m_s}{m_h - m_i} \quad (2)$$

$$\rho_s = \frac{m_s}{m_s - m_i} \quad (3)$$

$$WA = \frac{m_h - m_s}{m_s} \quad (4)$$

With:

- Φ: the open porosity in % of the sample volume.
- ρ_b: the bulk density of the sample in g.cm^{-3}.
- ρ_s: the skeletal density of the sample in g.cm^{-3}.
- WA: the water sorption coefficient by mass in the sample.
- m_s, m_i and m_h: respectively, the dry mass, the immersed mass and the saturated surface dried mass of the sample.

2.3. Accelerated carbonation experiments

Samples measuring 3.5 x 3 x 2.5 cm³ were first pre-conditioned in a desiccator filled with NH_4NO_3 salt to achieve a relative humidity (RH) of 63%. NH_4NO_3 was selected to maintain the RH within the optimal range of 50-75%, ensuring the ideal condensed water content in the cement matrix for carbonation. The carbonation experiments on the mortar samples were conducted under accelerated conditions at atmospheric pressure and ambient temperature using a BINDER CB 150 CO_2 chamber, with the CO_2 concentration set to 1%. The experiment lasted for 30 days over several composites of each formulation carbonated in parallel. Two or three samples were taken at the same time at 0, 7, 14, 20, and 30 days of carbonation and split into two pieces in order to collect the maximum amount of data to provide reliable averages of CO_2 uptake and different textural and chemical properties. The samples carbonated for 30 days were also used for post-mortem characterizations via MIP measurements, and the biochar particles were extracted for characterization through TPD-MS measurements.

2.4. Quantification of CO_2 uptake

To evaluate carbonation evolution, carbonation depth analysis was performed on the carbonated composite samples. The samples were split in half, and the exposed surfaces were sprayed with a phenolphthalein solution. The carbonation front was revealed as colorless (pH ≤ 10), while the uncarbonated front appeared purple (pH ≥ 12.5). Since one side of the composites was in contact with the carbonation chamber, CO_2 penetration on that side was hindered, resulting in slower advancement of the carbonation front. A digital processing of the images using ImageJ v1.53 software has been done for accurately assessing the percentage of carbonated areas [48]. The carbon-cement matrix interface was examined using optical microscopy with an Olympus BX51.

Quantification of the CO_2 uptake was accomplished through Temperature Programmed Desorption coupled with Mass Spectrometry (TPD-MS). Samples weighing 10–20 mg were placed in a

thermobalance and heated up to 1000 °C at a rate of 10 °C/min under an inert atmosphere (Argon, 100 mL/min). The decomposition products (gases evolved) were monitored in real-time using an online mass spectrometer (Skimmer, Netzsch).

2.5. Numerical modelling approaches

To understand the interface between the porous biochar and the cement matrix under CO_2 diffusion, numerical modelling was conducted across two scales: macro and atomistic. The macro-scale study was based on a two-phase model consisting of a biochar particle and the cement matrix. Utilizing a multi-reactional and time-dependent carbonation model [18], numerical simulations were performed using the Finite Element Method with the commercial software ComsolMP. The model considered a two-phase medium comprising one porous biochar particle and its surrounding cementitious matrix. CO_2 diffusion was assumed to occur only within the porous grain, while the cementitious matrix underwent carbonation. To more accurately reflect the surface roughness of the porous grain and its complex geometry, a 3D laser scan was performed to model the biochar particle, which was then incorporated into a rectangular cement prism measuring 2 cm x 1 cm x 0.5 cm. The mesh contained over 1 million elements, and the computation time lasted for 30 minutes using 121 processors and 512 GB of RAM.

The atomistic-scale study employed the Grand Canonical Monte Carlo algorithm [49,50]. The structure of the porous biochar was constructed based on experimental results from the structure factor and radial distribution function of a commercial carbon [51]. The 3D reconstruction was achieved using the Hybrid Reverse Monte Carlo method [52–55], incorporating a multi-staging process that included energy minimization, structure factor fitting, and constraints for three-membered rings [56]. Two layers of calcium silicate were generated using the Wollastonite structure through custom-written C++ code [57], which were then positioned adjacent to the activated carbon structure within periodic simulation boxes. Binary CO_2/water adsorption simulations were conducted using the Grand Canonical Monte Carlo algorithm [49,50].

3. Results and discussion

3.1. Composite materials preparation

Figure 1a summarizes the steps involved in manufacturing the composites. A detailed formulation of the composite materials is presented in Table 1. Type I was prepared as a reference material using recycled concrete aggregates (RCA). For Type II, 40% of the RCA volume was replaced with biochar particles of similar size, approximately 6 mm. Table 1 indicates that the amount of cement used is the same for both composites. However, to maintain an equivalent amount of effective water and the

water-to-cement (w/c) ratio, an additional volume of water was incorporated during the mixing process for the preparation of Type II.

LN 750 is a highly porous and hydrophilic biochar [58] that can sorb up to 746% of its weight in water (as shown in Table 2). Consequently, 68 mL of water was added during the preparation of the Type II composite to compensate for the water uptake by the porous biochar. As a result, the porous carbon does not absorb any additional water from the cement matrix and the rheology of the mix is maintained. Since the density of the biochar is lower than that of the RCA (see Table 2), the aggregate-to-cement (a/c) ratio is smaller for Type II, even though the volume of aggregates remains the same in both composites. After hydration, Figure 1 illustrates that the aggregates in both Type I and Type II are homogeneously distributed within the cement matrix.

3.2. Physico-chemical characterizations of materials and composites

The physicochemical characterization of the porous biochar particles was performed before their incorporation into the concrete formulation. From the point of view of porosity, the pyrolysis of seaweed stems and leaves results in the development of various pore size ranges, from microporosity to macroporosity. The porous texture of the biochar particles was analysed using nitrogen (N_2) and carbon dioxide (CO_2) gas adsorption to evaluate the micro- and mesoporosity, and mercury intrusion porosimetry (MIP) for assessing meso- and macroporosity. As illustrated in Figure 2a, the nitrogen adsorption isotherm for LN 750 exhibited a Type IV isotherm shape, characterized by a hysteresis loop between the adsorption and desorption curves. The gradual gas adsorption observed at a relative pressure (P/P_0) of less than 0.1 is associated with volume filling in micropores, while the hysteresis at higher pressures corresponds to gas condensation in mesopores [25,59]. The BET specific surface area calculated was 1324 m^2/g, and the NLDFT pore size distribution (Figure 2b) revealed a significant portion of pores within the micropore range ($d < 2$ nm), with a pore volume of 0.4 cm^3/g. Additionally, another peak was detected in the mesopore range between 2 and 10 nm, corresponding to a pore volume of 0.35 cm^3/g.

From the CO_2 adsorption isotherm obtained on LN 750 at 273 K, the volume of micropore with diameters smaller than 0.7 nm, as determined by the Dubinin-Radushkevich equation, was equal to 0.4 cm^3/g. These results indicate that microporosity under 0.7 nm is even more developed than the larger microporosity and mesoporosity present in the biochar. This porosity was developed during the pyrolysis in reason of the presence of alkaline earth metals in the seaweed promoting a process of so-called self-activation [45]. This kind of microporosity with pore diameters of ca. ~ 0.65-0.8 nm were reported as optimal for CO_2 storage [24].

The larger mesoporosity and macroporosity of the biochar were determined using MIP. The pore size distribution shown in Figure 2c reveals a broad peak in the pore range between 300 nm and 3 µm, with a maximum around 1 µm. The macropore volume was measured at 2.42 cm^3/g. This macroporosity is

attributed to the parent cellular structure of the seaweed prior to pyrolysis. Table 2 indicates that the biochar exhibits a total open porosity of 49%, as determined by mercury intrusion, along with a low bulk density of 0.15 g/cm³. The apparent porosity and bulk density can also be assessed through water sorption. As mentioned in the previous section, LN 750 particles can sorb approximately 750 wt% of water due to their highly developed porosity, which is further enhanced by their hydrophilic nature. In fact, LN 750 contains a significant amount of oxygen surface functional groups (see TPD-MS in Figure S1 of the supporting information), providing an hydrophilic character to the carbon surface [58]. Table 2 demonstrates that the open porosity for water sorption in LN 750 reached as high as 92.6 wt%, corresponding to a bulk density of 0.12 g/cm³ and a low skeletal density of 1.69 g/cm³.

Figure 2c illustrates the pore size distribution obtained through MIP for Type I and Type II samples after hydration, assessing the impact of LN 750 on composite porosity. Cement materials typically exhibit various pore types, ranging from approximately 0.001 μm to over 1000 μm [60,61]. The smallest pores, known as gel pores, range roughly from 0.001 to 0.01 μm and correspond to voids created during hydration by the formation of colloidal Calcium Silicate Hydrates (CSH) particles. These are followed by capillary pores, which range from 0.01 to 1 μm, corresponding to the spaces originally occupied by water among the anhydrous cement particles. These spaces become vacant as cement hydrates form during hydration [62]. As hydration progresses, capillary pores tend to decrease in volume and size as more spaces are filled with cement hydrates, particularly CSH, while the overall volume of gel pores increases. Additionally, a small fraction of porosity can be attributed to air voids that become entrapped in the paste during mixing and casting, typically ranging from 10 μm to over 10000 μm. Unlike gel and capillary pores, which form an interconnected network with channels linking them, air voids are generally isolated from each other and thus cannot be detected by MIP; they do not contribute to liquid or gas transport.

In cement paste, cement particles are usually packed randomly during mixing, creating a homogeneous pore size distribution throughout the structure during hydration. For mortars and concrete materials, the introduction of millimetre-scale aggregates in the mix induces “wall effects,” resulting in a rearrangement of the cement particles. In this arrangement, smaller particles tend to pack closely against the aggregate surfaces, while larger ones are located further away [63]. Some researchers have suggested that micro-bleeding effects occur during mixing [64,65], which refer to the accumulation or entrapment of mixing water around the aggregate surfaces. The combination of wall effects and micro-bleeding creates interfaces between the cement matrix and the aggregate surfaces, leading to a higher water-to-cement (W/C) ratio than that of the bulk paste. This results in increased porosity, as a lower cement content combined with higher water content expands and enlarges the capillary voids formed during hydration. According to Elsharief et al. [66], both the size of the aggregates and the initial W/C ratio influence this interface porosity: smaller aggregates and lower W/C ratios correlate with reduced

porosity at the interface. The width of these interfaces typically matches the size of the cement particles, usually not exceeding 20-50 μm [63].

Figure 2c indicates that the pore sizes for Type I and Type II are primarily distributed within the range of 0.006 to 0.3 μm. Some of the porosity in these materials appears to be attributed to the recycled concrete aggregates (RCA), as shown in Figure 2c, which also displays pores in the 0.006-0.3 μm range. This porosity is associated with the capillary porosity of the old hardened cement paste remaining on the aggregates, exhibiting a significant distribution in the 0.006-0.01 μm range compared to the 0.02-0.3 μm range. This may suggest that the old hardened cement paste has undergone partial carbonation, as clogging in some areas of the capillary porosity could lead to a reduction in pore size (see quantification in Table 2). Indeed, hydrostatic weighing revealed that the RCA had bulk densities and water sorption of 2.41 $g.cm^{-3}$ and 4.5%, respectively (Table 2). These results align closely with those obtained by Zhang et al. [67] on carbonated RCA and are comparable to findings on natural aggregates, confirming that the RCA used in the formulations was already significantly carbonated. Consequently, the capillary porosity observed in Type I material was derived from both the RCA and the cement used to prepare the composite.

For the Type II materials, which contain the same amount of cement as Type I but have part of the RCA aggregates replaced with biochar particles, Figure 2c shows that the pores in the range of 0.006-0.3 μm are distinctly more developed, leading to increased capillary porosity (Table 2). The capillary porosity in the Type II composite reached 14.9%, compared to 9.5% for Type I. Furthermore, Figure 2c reveals an additional peak in the 0.3-4 μm range for Type II. By comparing this with the pore size distribution of LN 750, it is clear that this peak corresponds to the porosity of the added carbon. Thus, incorporating porous biochar into the formulation significantly influences material porosity. The increase in capillary porosity, coupled with the emergence of new porosity in Type II, results in a total porosity of 30.5%, as opposed to 13.3% for the material without carbon. Table 2 also indicates that adding low-density biochar reduces the density of the composites.

The results obtained from hydrostatic weighing (HW) experiments on the Type I and Type II composites reveal a notable effect of biochar addition on open porosity (Φ), bulk density (ρb), skeletal density (ρs), and water sorption capacity (WA). The open porosity obtained through water sorption shows an increase similar to that observed with mercury intrusion upon adding the porous carbon. The open porosity percentage for Type II reached 35.5%, compared to 18.2% for Type I. Such an increase in porosity cannot be solely attributed to the addition of porous carbon material with 92.6% porosity, as the weight percentage of biochar in the composite is only 1.2% of the total weight (Table 1). Therefore, a more developed capillary porosity will also contribute to the higher open porosity in Type II. Considering that LN 750 can sorb over 700 wt% of water, additional water was introduced during the preparation of Type II to maintain the same W/C ratio as Type I. However, it is possible that some of the added water is desorbed from the biochar into the cement matrix during hydration [68,69].

Compared to Type I, this water desorption, coupled with wall and increased bleeding effects, could lead to a local increase in the W/C ratio at the interface with the cement matrix, similar to the interactions at the aggregate-cement interfaces. Such phenomena could explain the more developed network of capillary pores observed in Type II after hydration (Figure 2c, Table 2). This factor, along with the addition of low-density biochar, reduces both the bulk density and skeletal density of the material. The creation of new porosity in the composite materials also significantly influences water uptake, as shown in Table 2. The Type II composite could sorb 21.5% of water, more than double the amount sorbed by Type I. In summary, the incorporation of porous biochar has a substantial effect on the textural properties of the composite and its water sorption capacity. Consequently, the carbonation process is likely to be affected.

To determine whether the presence of biochar affects the amount of carbonatable compounds during the mixing and hydration of the composites, Temperature-Programmed Desorption coupled to Mass Spectrometry (TPD-MS) was conducted to investigate and quantify their chemical composition. Figure 3 illustrates the weight losses and the gases released from room temperature up to 900 °C.

From room temperature to approximately 300 °C, a significant weight loss occurs, associated with the release of H_2O. This H_2O release results from both sorbed water and the thermal decomposition of Calcium Silicate Hydrates (CSH) and tri- or mono-substituted aluminate ferrite phases (AFt/AFm), such as ettringite. The weight loss for Type I in this temperature range was 8.4 wt%, while for Type II, it averaged 12.8 wt%, corresponding to 4669 µmol $H_2O \cdot g^{-1}$ and 7113 µmol $H_2O \cdot g^{-1}$, respectively. Given the higher water sorption capacity of the Type II composite (as shown in Table 2), these differences likely arise from the desorption of sorbed H_2O within the porosity of the composite.

The weight loss observed in the range of 400-550 °C is also associated with H_2O release, corresponding to the dehydration of $Ca(OH)_2$. The weight loss linked to H_2O evolution was 3.8 wt% for Type I and 4.4 wt% for Type II, indicating a higher amount of the $Ca(OH)_2$ phase in Type II, likely located at the cement/biochar interface due to its preferential precipitation in the carbon-cement interfaces [65].

Finally, the weight loss in the range of 600 °C to 900 °C corresponds to CO_2 release from the thermal decomposition of $CaCO_3$. The weight loss associated with $CaCO_3$ indicated that the Type I composite contained 2.6 wt% of CO_2, while the amount in Type II was approximately 3.7 wt%. These small amounts correspond to the carbonation of recycled concrete aggregates (RCA) and the composite itself. The differences observed by TPD-MS on hydrated and carbonated phases in the Type I and II composites has been confirmed by XRD (Figure S2a). The evolution of these different phases during carbonation will be monitored by TPD-MS.

3.3. Accelerated carbonation of composites

Composite material samples were carbonated under accelerated conditions using an incubator with 1% CO_2 and 65% relative humidity (RH) for up to 30 days. Multiple sample batches were carbonated simultaneously to conduct carbonation depth analysis and quantify CO_2 uptake using TPD-MS.

Figure 4 illustrates the carbonation depths of samples subjected to varying time intervals, determined by spraying a phenolphthalein solution, which allowed for monitoring pH changes following CO_2 gas penetration and the carbonation of hydrates. The figure indicates that the extent of the carbonated surface of the composite—represented by the uncolored regions—increases more rapidly over time for the sample containing biochar. Specifically, the depth measurements reveal that the carbonation reaction appears to be enhanced in the vicinity of the porous biochar particles. These observations clearly demonstrate that biochar positively influences CO_2 diffusion within the cement matrix. After 30 days of carbonation, the carbonated surface of the Type I composite was estimated through the analysis of several specimens for each material carbonated in parallel, to cover approximately 78% of the total surface, compared to around 95% for Type II.

The evolution of the cement phases during carbonation was analyzed using TPD-MS, which combined data obtained from weight loss and the gases released during heat treatment. From the H_2O and CO_2 released as the temperature rises, the contributions to weight loss due to the thermal decomposition of the hydrates and carbonates can be quantified and separated, as shown in the previous section for the composites after hydration. The interest in the use of TPD-MS instead of thermogravimetric analysis (TG or DTG) alone is more evident in the analysis of carbonated materials. TPD-MS allows to quantify the cement phases more accurately, since hydrates such as $Ca(OH)_2$ and some amorphous carbonates can decompose in similar temperature ranges, contributing together to the same TG-DTG peak. Figure 5 shows the loss of weight in % and the evolution of the H_2O and CO_2 gas in µmol/g/s in relation to the respective loss of mass. Figure 5a present the TPD-MS at different carbonation times for the Type I material and Figure 5b for the Type II material containing the biochar. Figures 5a and 5b depict a general trend characterized by a decrease in H_2O evolution alongside an increase in CO_2 release throughout the carbonation process. This aligns with the transformation of hydrated phases into carbonated ones. The gas evolution profiles for both materials indicate that at the onset of carbonation, there is primarily the consumption of $Ca(OH)_2$, correlating with the H_2O peak observed between 400-500°C, which produces crystallized $CaCO_3$ in its calcite polymorph, corresponding to the CO_2 peak detected between 700-800°C. As carbonation progresses, CO_2 evolution shifts to lower temperatures due to the carbonation of C-S-H (calcium silicate hydrate) and Afm/Aft phases, leading to the formation of amorphous or poorly crystallized $CaCO_3$ [70,71] that decomposes between 400-700°C [72–74]. The carbonation of C-S-H also results in the emergence of vaterite and aragonite $CaCO_3$ polymorphs [70], which decompose in the same temperature range as amorphous and poorly

crystallized calcite as described by Vogler et al. [72]. The presence of the different $CaCO_3$ polymorphs has been confirmed by XRD (Figure S2b).

A closer examination of the CO_2 evolution peaks, comparing those from the reference material and the composite containing biochar (Figure 6a), reveals that for a given number of carbonation days, the amount of CO_2 evolved is consistently higher for the composite with biochar. Over the first seven days of carbonation, both materials exhibit a predominant increase in the peak at 700-800°C associated with the formation of calcite-like $CaCO_3$, with a more significant increase noted for the material containing biochar. As carbonation days increase, the reference Type I material (dotted lines in Figure 6a) shows a steady evolution of CO_2 related to the formation of calcite-like $CaCO_3$, with further carbonation only resulting in an increase of amorphous or less crystalline $CaCO_3$ decomposing between 400-700°C. In contrast, for the Type II composite material with biochar, the amount of all carbonated phases—both crystallized and more amorphous—continuously increases throughout the carbonation process. Thus, the presence of porous biochar also influences the chemical composition of the carbonated phases.

After quantifying the H_2O and CO_2 evolved from the thermal treatment of the composites over different carbonation durations, Figure 6b confirms that the decrease of hydrated phases and the CO_2 uptake, expressed as mass percentage considering the total mass of material, are more pronounced in the Type II composite containing the porous biochar. To demonstrate that this enhanced CO_2 uptake is not related to a decrease in the density of the material due to the inclusion of low-density biochar (see Table 2), Figures 6c and 6d illustrate the evolution of CO_2 uptake through carbonation based on material volume (Figure 6c) and exposed surface area (Figure 6d), respectively. It was observed that both materials exhibited roughly similar CO_2 uptake per material volume or accessible surface at seven days; however, the CO_2 uptake progressed more rapidly for the porous biochar Type II composite compared to the reference Type I composite as carbonation days increased.

The results clearly indicate that the addition of porous biochar positively influences both carbonation kinetics and the amount of CO_2 uptake. These findings align with the carbonation fronts shown in Figure 4. Carbonation phenomena in concrete materials primarily depend on CO_2 gas diffusion, followed by solubilisation in condensed water and subsequent reaction with the cement hydrates. As previously reported, the Type II composite with biochar exhibits a different porosity compared to the Type I reference composite. Indeed, different types of diffusion regimes occur within the cement's porosity based on pore sizes. For gel pores with a diameter of $d < 0.008$ µm, the Knudsen diffusion regime is dominant, as the pore diameter is significantly smaller than the mean free path (λ) of CO_2 molecules, which is approximately 84 nm ($d < \frac{\lambda}{10}$). In these conditions, CO_2 diffusivity is proportional to the average molecular speed of CO_2 and the pore radius. Additionally, surface diffusion may also occur in the smallest gel pores, where CO_2 molecules diffuse along the pore through successive adsorption-desorption reactions on adjacent active sites via Van der Waals interactions [14,75].

Conversely, molecular diffusion prevails for pores with diameters greater than 0.8 μm, as the diameter exceeds the mean free path of CO_2 molecules by a factor of ten. In this case, CO_2 diffusivity depends solely on molecular speed and the mean free path of CO_2 molecules. For pores ranging between 0.008 and 0.8 μm, both Knudsen and molecular diffusion regimes coexist. Overall, the effective diffusivity of a cement paste can be estimated as the sum of the various diffusion regimes occurring in proportion to their respective porosity fractions [76]. As indicated by the mercury intrusion porosimetry (MIP) measurements, the incorporation of porous biochar into the cement matrix significantly increases the capillary pore volumes between 0.006-0.3 μm, along with the additional macropore volumes introduced by the own macroporosity of the biochar. The increase in these pore volumes likely enhances the contributions of the mixed Knudsen and molecular diffusion regime in the capillary range, as well as the molecular diffusion regime in the macroporous range, leading to higher effective diffusivity in the composite compared to the reference material, which has a lower capillary porosity fraction and minimal porosity beyond 0.4 μm.

It is also important to note that carbonation itself impacts pore connectivity and CO_2 gas diffusion in cement-based materials. The change in porosity during carbonation depends on the composition of the material, specifically the type of cement and the inclusion of supplementary cementitious materials [17,77]. If the C-S-H content is high, carbonation can induce an increase in porosity as porous silica gel is generated [77]. However, in our case, the high content of $Ca(OH)_2$ in Portland cement generally leads to a reduction in pore size and porosity during carbonation [17]. The decalcification of $Ca(OH)_2$ to produce $CaCO_3$, which precipitates in the pores, results in an increase in solid volume, as the molar volume of $CaCO_3$ is greater than that of $Ca(OH)_2$. In this context, Type I and Type II composites were characterized after 30 days of carbonation using MIP, and the results were compared to those obtained from the uncarbonated samples. Figure 7 confirms that, compared to the uncarbonated samples, pore distribution after carbonation evolves towards a reduction in larger capillary pores while an increase in smaller capillary pores is observed in both Type I and Type II composites. As discussed earlier, this result may be linked to the formation of $CaCO_3$ during carbonation, which precipitates over the pore walls and reduces pore diameters, thereby shifting the distribution towards smaller capillary pores. The increased mercury volume obtained from the 30-day carbonated Type II sample also indicates a significant reduction of approximately 1 μm corresponding to the biochar macroporosity. This may suggest a clogging effect of the pore walls caused by carbonated products diffusing into the biochar particles and obstructing porosity. Overall, the reduction in capillary porosity due to carbonation was notably more pronounced in the Type II composite. Figure 7b presents capillary porosities calculated from the mercury-intruded volumes in the range of 5 to 300 nm relative to the total intruded mercury volumes in the samples. Results indicate that capillary porosity in Type I decreased from an average of 9.5% to 8.2%, while it decreased from 14.9% to 11.1% in Type II. This indicates that the relative porosity reduction for Type II is approximately three times higher than that for Type I, suggesting that

carbonation was more effective in the Type II composite, consistent with the observations of carbonation depths in the 30-day carbonated samples. Nevertheless, the porosity of the composite containing porous biochar remains significantly higher than that of the reference Type I composite, even after carbonation. Thus, the improved carbonation efficiency observed for the composite with biochar (Figure 6) can also be attributed to the more developed capillary pore network, which facilitates enhanced CO_2 diffusion rates.

To investigate the effect of biochar addition on CO_2 diffusion within the cement matrix, the CO_2 diffusivity (DCO_2) was calculated from the experimental data on CO_2 uptake presented in Figure 6c. According to Yang et al. [78], the CO_2 uptake during cement matrix carbonation in concrete structures can be correlated with the total amount of absorbable CO_2 through carbonation in the cement and the carbonation depth at time t, expressed by the following equation:

$$U_{CO_2}(t) = a_{CO_2} \cdot x_c(t) \quad (5)$$

With:

- U_{CO2} (t) (g.cm^{-2}), the CO_2 uptake in the concrete at carbonation time t
- a_{CO2} (g.cm^{-3}) the total amount of CO_2 fixed in the concrete by $CaCO_3$ formation
- x_c (t) (cm), the carbonation depth at carbonation time t

According to the authors, x_{CO2} (t) can be theoretically calculated from a_{CO2}, the CO_2 gas diffusion coefficient in the concrete and the atmospheric CO_2 concentration with the following equation:

$$x_{CO_2}(t) = \sqrt{\frac{2D_{CO_2} \cdot C_{CO_2}}{a_{CO_2}} \cdot t} \quad (6)$$

Incorporating equation (6) in (5), $U_{CO2}(t)$ can be expressed as a time square root equation including a slope A, such as :

$$U_{CO_2}(t) = a_{CO_2} \cdot \sqrt{\frac{2D_{CO_2} \cdot C_{CO_2}}{a_{CO_2}}} \cdot \sqrt{t} = A \cdot \sqrt{t} \quad (7)$$

As illustrated in Figure 8a, the experimental CO_2 uptake for both Type I and Type II composites (from Figure 6c) was fitted to the square root of carbonation time, represented by solid blue and red lines for Type I and Type II, respectively. This fitting allowed for the determination of the slopes for both composites (denoted as AT−I and AT−II). The experimental CO_2 diffusivity (DCO_2) was calculated using equation (7), while the theoretical aCO_2 was derived from the water-to-cement (W/C) ratio, hydration time, and cement content in the composite materials, following the equations provided by Yang et al. [78]. Detailed calculations can be found in the Supplementary Information. The experimental DCO_2(t) for Type I was measured at 3.2×10^{-8} m²/s, aligning with literature values for similar test conditions and compositions [21,79]. For Type II, the experimental DCO_2 was 6.2×10^{-8}

m^2/s. This higher diffusivity coefficient in Type II, confirms that the presence of biochar particles enhances effective CO_2 diffusivity within the cement matrix.

To gain understanding on such a positive effect of biochar addition on CO_2 diffusion within the cement matrix, numerical simulations were conducted with a CO_2 gas flow passing through a composite sample, which was reconstructed digitally and included a scanned biochar particle (Figure 8b) embedded in a cement matrix (Figure 8c). In this model, unidirectional CO_2 gas flow diffusion was utilized, necessitating the application of symmetry boundary conditions around the specimen. The Dirichlet boundary condition was imposed solely on the external surface exposed to a 1 vol% concentration of CO_2, while the opposite side of the outer surface was left free, allowing the CO_2 gradient to influence the flow direction.

The time-dependent evolution of the CO_2 concentration gradient was calculated every second for up to 10 hours. For comparison, simulations were also performed on a numerical sample devoid of biochar, with the porosity of the cement matrices in both numerical samples set to match those observed in the uncarbonated samples of Types I and II. Figures 8d and e illustrate the CO_2 flow (represented as arrows) traversing the Type II composite after 10 hours and the CO_2 concentration (represented in by colours from hot to cold when reducing concentration).

The numerical simulation reveals that the presence of the biochar particle in the cement matrix influences the CO_2 flow velocity and direction. As shown in Figure 8d and more clearly in the zoom of Figure 8e, the simulation reveals that the direction of the diffusing CO_2 gas flow changes dramatically, suggesting that the gas is adsorbed by the biochar particle. Specifically, the LN 750 biochar exhibits a CO_2 storage capacity (determined from the CO_2 adsorption isotherm at room temperature, Figure S3) as high as 158 $mgCO_2.g^{-1}$, in reason of its highly developed microporosity presenting the optimal pore size for CO_2 adsorption. This value is much higher than that obtained with other raw biochars, or even with biochars that have undergone additional post-treatment to modify their surface and/or porous texture to increase their capacity to adsorb CO_2 [31]. Due to such important adsorption of CO_2 into the microporosity of the biochar, the CO_2 flow originating from the surface decelerates more rapidly as it approaches the biochar, which reduces the concentration at the entrance of the pores. The flow then accelerates significantly within the biochar, owing to its high meso- and macroporosity. Consequently, the flow emerges on the opposite side with a velocity exceeding that in the cement matrix, as the elevated CO_2 concentration within the porosity of the biochar would establish a new gradient towards the bulk. The vector of the entering flow is directed toward the biochar and distributed in a homogeneous manner around the particle. Ultimately, the flow direction shifts from unidirectional to perpendicular to the grain, i.e., a circumferential direction for enhanced diffusion. Therefore, when the gas flow passes through such a highly porous medium, it subsequently diffuses in all directions around the particle (see "vector" arrows in Figure 8d and e), resulting in an increase in the CO_2 concentration in the vicinity of the biochar particle. The last is illustrated in Figure 8f presenting the distribution of

the CO_2 concentration gradient on the cutting plane through the centre of the numerical composite sample (0 mm stands for the composite surface) at 1 second, 10 seconds, and 10 hours for the Type II composite in comparison to the Type I. For the Type I the CO_2 concentration decrease continuously from the surface to the bulk of the material because the CO_2-hydrates reaction. However, for Type II, the concentration decreases more rapidly in the vicinity of the carbon particle because the adsorption of CO_2 at the biochar microporosity, tends to diffuse rapidly through the carbon porosity and exit the particle at a higher concentration than for the Type I composite at the same carbonation time (10 s or 10 h).

This influence of biochar particles on CO_2 flow velocity and direction, which enhances CO_2 concentration at the interface with the cement matrix, was further corroborated by optical microscopy analysis. Figure 9 shows images of the biochar-cement interface in the Type II composite before and after 30 days of carbonation. Figure 9a indicates that the biochar particles are well integrated into the cement matrix, exhibiting good adhesion. The surface properties of the porous biochar, which contain a significant number of polar functional groups, promote the epitaxial growth of cement hydration products on the biochar surface through chemical reactions between the cement and biochar particles, thus enhancing adhesion between the matrix and aggregates [80]. In Figure 9b, a milky-colored layer was observed at the biochar interface in the 30-day carbonated sample, contrasting sharply with the rest of the cement matrix. This layer corresponds to the carbonation front depicted in Figure 4, where carbonation initiates around biochar particles as the carbonation front reaches them. Thus, considering previous studies [35], the milky layer in Figure 9b is attributed to the formation of $CaCO_3$, which creates a highly carbonated layer around the biochar particles. This observation aligns with the numerical simulations, suggesting that the CO_2 concentration gradient generated by CO_2 movement through the biochar towards the cement matrix fosters the formation of a dense $CaCO_3$ layer in the vicinity of the biochar, as more CO_2 becomes available for carbonation.

Optical microscopy, as shown in Figure 9b, also reveals the same milky solid deposition within the macroporosity of the biochar. The biochar particles were extracted from the composite after 30 days of carbonation and the core of the particle was sampled to perform a TPD-MS analysis. Figure 9c presents the weight loss and the amount of H_2O and CO_2 gases evolved during the thermal treatment in an inert atmosphere of the biochar extracted from the composite after 30 carbonatation days compared to the raw biochar. The biochar from the carbonated composite presents a weight loss in the 700-800°C range associated with CO_2 evolution, which was not present in the raw biochar. These results suggest the presence of amorphous or poorly crystallized $CaCO_3$ within the porosity of the biochar. The precipitation of $CaCO_3$ in the porosity of the biochar is supported by a reduction in porosity in the 0.3-1 μm range, associated with the presence of the biochar in the composite, as observed through mercury intrusion porosimetry (MIP) (Figure 7a). After 30 days of carbonation, porosity decreased from 10.2% to 3.8% in this range (Table 3). These findings confirm that biochar provides a suitable

environment for the deposition of carbonation products. The contribution of $CaCO_3$ deposited inside the porosity of the biochar to the total carbonation products accounts for the pronounced shoulder seen in the CO_2 evolution profile after carbonation between 600-700°C (Figure 9c), which is nearly absent during the carbonation of the Type I composite without biochar (Figure 6a).

Grand Canonical Monte Carlo (GCMC) simulations were conducted to further investigate the cement matrix/carbon interface during carbonation. Figure 10a illustrates the interface between cement, predominantly containing CSH, and carbon. In the presence of 1% CO_2 (10,000 ppm) and 65% relative humidity, Figure 10b shows that CO_2 molecules preferentially occupy the inter-layer spaces between CSH layers and the interface zone between CSH and carbon. Simultaneously, a large number of water molecules are adsorbed into the porosity of the carbon, and an interfacial water layer forms between the CSH and carbon, as depicted in Figure 10c. Thus, in addition to the substantial amount of water near the biochar particles, which affects hydration and matrix porosity development through bleeding effects, the biochar porosity also contains a significant amount of water.

Consequently, the high concentration of water and CO_2 at the cement/biochar interface and within the porous network can explain the presence of $CaCO_3$ inside the porosity of the biochar and the dense $CaCO_3$ layer surrounding the biochar particles. This phenomenon can be paralleled with CO_2 geological sequestration [81]. It is well established that carbonate chemical weathering in aquatic ecosystems, including oceans, consumes atmospheric CO_2. Specifically, the dissolution of calcite in CO_2-containing water is crucial in many geological processes and serves as a significant atmospheric CO_2 mitigation strategy. The sculpting of karst landscapes and caves in limestone terrains or the formation of stalactites, stalagmites, columns, and other speleothems in caves are among the most remarkable examples [82]. In nature, when a high concentration of dissolved CO_2 interacts with rocks containing $CaCO_3$, the following reactions have been extensively studied and documented [83–87]:

$$CaCO_3 + CO_2 + H_2O \rightarrow Ca(HCO_3)_2 \quad (8)$$

Under conditions of high CO_2 concentrations, Reaction (8) will proceed in the forward direction, leading to the dissolution of solid $CaCO_3$. Conversely, when the amount of dissolved CO_2 in water decreases, the backward reaction will generate solid $CaCO_3$, facilitating the formation of speleothems, as previously described.

During the carbonation process in composites, in addition to the presence of CO_2, the conditions are also characterised by a high water content in the porosity, which would allow reaction (8) to take place over the calcite produced during carbonation. Notably, in cementitious materials containing portlandite, Reaction (8) would be predominantly forward. This could happen because the calcium bicarbonate solution can react with $Ca(OH)_2$ to regenerate calcite, as shown by the following reaction:

$$Ca(HCO_3)_2 + Ca(OH)_2 \rightarrow 2CaCO_3 + 2H_2O \quad (9)$$

Reaction 8 will be particularly favored in the vicinity of biochar particles where there is a high local water content, as determined by molecular dynamics (MD) simulations (Figure 10). This reaction is also promoted by high CO_2 concentrations, as indicated by modelling (Figure 8), and elevated levels of $Ca(OH)_2$, confirmed by TPD-MS analysis (Figure 6). Consequently, reaction (8) will lead to an increased consumption of $Ca(OH)_2$, since the formation of $CaCO_3$ on the surface of portlandite inhibits further diffusion of CO_2, significantly impacting the kinetics of carbonation. The weathering of $CaCO_3$ results in a greater conversion of $Ca(OH)_2$ to $CaCO_3$ because the higher solubility of $Ca(HCO_3)_2$ and its diffusion in the water present at the cement/biochar interface enhances CO_2 diffusion throughout the bulk of the particle. This assertion is supported by quantifying the $Ca(OH)_2$ consumption during carbonation, as demonstrated by integrating the H_2O gas evolution between 400 and 700°C in the TPD-MS measurements presented in Figure 6c. For the composite containing biochar, the amount of consumed $Ca(OH)_2$ consistently increases over the carbonation period, whereas for the Type I composite, the amount of $Ca(OH)_2$ consumed shows minimal change after 7 days of carbonation. These results align with the observations in Figure 6a, where the products of $Ca(OH)_2$ carbonation—specifically, crystallized $CaCO_3$ that decomposes to release CO_2 gas around 700-800°C—increased for the Type II composite during carbonation, while no significant growth was observed for Type I after 7 days.

Moreover, the presence of $CaCO_3$ within the porosity of the biochar particles suggests that they play a critical role in the aqueous diffusion of species through the water layer at the biochar-cement interface. The precipitation of $CaCO_3$ within the biochar could indicate that hydration products and calcite weathering products are diffusing into the porosity to react according to the reaction (9). The reaction nature-inspired mechanism that we propose here is illustrated in the scheme in Figure 11. All the results presented above confirm that, in addition to influencing the matrix microstructure and CO_2 diffusion, highly porous biochar particles actively participate in CO_2 uptake through both physical and chemical mechanisms. Beyond the physisorption of CO_2 in the micropores, evidence exists for the precipitation of $CaCO_3$ within the meso- and macroporosity as it has been previously observed by Gupta et al. when using biochars with small surfaces areas presenting mainly macroporosity [35].

Overall, the biochar particles distributed within the cement matrix act as reservoirs for water and CO_2, significantly impacting material hydration and carbonation. The incorporation of biochar into a cement-based material enhances both the kinetics of carbonation and the degree of carbonation of carbonatable hydrates.

Nevertheless, those results should be confirmed by using formulations of construction materials and in natural carbonation conditions.

4. Conclusions

This study presents an effective and sustainable strategy to address the slow carbonation kinetics of cement-based materials while simultaneously increasing CO_2 uptake capacity. The introduction of highly porous biochar particles into the formulation facilitates the valorisation of recycled concrete aggregates (RCA) into a composite material that efficiently captures CO_2.

The porous biochar obtained from the pyrolysis of seaweeds exhibits interesting textural properties, characterized by a highly developed specific surface area, including micropores with optimal pore size for CO_2 adsorption together with mesopores and macropores, along with a significant presence of oxygen surface functionalities. These features confer both gas adsorption and hydrophilic properties to the biochar, promoting the adsorption of substantial amounts of CO_2 and the uptake of important amounts of liquid water. As a result, the carbon particles dispersed within the cement matrix, in conjunction with the RCA, serve as effective reservoirs for water and CO_2, having a main role during material hydration and carbonation.

The porous nature of biochar significantly impacts porosity development during hydration. It can uptake over 700 wt% of water, and Grand Canonical Monte Carlo (GCMC) simulations indicate that this water is primarily located within the porosity of the biochar and at the carbon/cement interface. This substantial volume of water adjacent to the biochar particles affects hydration and matrix porosity development through bleeding effects, leading to the enhanced formation of capillary pores. The combination of this capillary porosity and the macropores of the biochar results in an open porosity of 30.5%, compared to only 12.3% for the composite without biochar. Furthermore, the introduction of biochar increases water uptake from 8.5 wt% to 21.5 wt%.

These physico-chemical changes induced by the addition of porous biochar to the cement matrix, in addition to the intrinsic porosity of the biochar, have a significant positive impact on both carbonation kinetics and CO_2 uptake. Employing a combined experimental and simulation approach, the observed faster kinetics for the biochar-enhanced composite can be attributed to a higher effective CO_2 diffusivity. The greater porosity of the Type II composite increases both Knudsen and molecular diffusion rates. In addition, the CO_2 adsorption properties of the biochar conferred by its microporosity acted as a driving force to redirect the flow of CO_2 traversing the biochar from the sample surface to around the biochar surface, allowing deeper penetration into the concrete thickness.

The increased CO_2 uptake exhibited by the composites with biochar is associated with the formation of a dense carbonated layer at the carbon-cement interface and the presence of $CaCO_3$ within the biochar porosity. Indeed, the CO_2 and H_2O-rich environment at the carbon/cement interface enhances the carbonation degree of the carbonatable hydrates by solubilizing the $CaCO_3$ layer formed during carbonation, which limits further CO_2 diffusion through the bulk of the particle. The weathering of $CaCO_3$ leads to the formation of highly soluble $Ca(HCO_3)_2$, which diffuses in the water contained in

the cement/biochar interface to react with additional $Ca(OH)_2$ and CO_2. This secondary carbonation reaction could explain the production of additional $CaCO_3$ that precipitates within the matrix and inside the biochar porosity. This specific mechanism shifts the carbonation equilibrium toward deeper carbonation of the bulk cement hydrates, explaining the increase of both the carbonation rate and CO_2 uptake in the presence of a highly porous biochar.

In conclusion, the incorporation of a biochar with a porous texture adapted to high CO_2 and H_2O uptake into cement-based materials improves the carbonation kinetics and increases the degree of conversion of carbonatable hydrates, thus positioning concrete as a viable material for CO_2 capture.

Acknowledgements

The authors thank the Région Centre val de Loire (Project APR-IA PRESERVE convention n°2019 00134933 and co-financement bourses doctorales 2020) and the ESTP-IR for financial support.

References

[1] H. Ritchie, M. Roser, P. Rosado, CO_2 and Greenhouse Gas Emissions, Our World in Data (2020). https://ourworldindata.org/co2-and-greenhouse-gas-emissions.

[2] I. Pigliautile, G. Marseglia, A.L. Pisello, Investigation of CO_2 variation and mapping through wearable sensing techniques for measuring pedestrians' exposure in urban areas, Sustainability 12 (2020) 3936. https://doi.org/10.3390/su12093936.

[3] P. Carreiro-Martins, A.L. Papoila, I. Caires, S. Azevedo, M.M. Cano, D. Virella, P. Leiria-Pinto, J.P. Teixeira, J. Rosado-Pinto, I. Annesi-Maesano, N. Neuparth, Effect of indoor air quality of day care centers in children with different predisposition for asthma, Pediatr. Allergy Immu. 27 (2016) 299–306. https://doi.org/10.1111/pai.12521.

[4] C. Kim, D. Choi, Y.G. Lee, K. Kim, Diagnosis of indoor air contaminants in a daycare center using a long-term monitoring, Build. Environ. 204 (2021) 108–124. https://doi.org/10.1016/j.buildenv.2021.108124.

[5] M. Simoni, I. Annesi-Maesano, T. Sigsgaard, D. Norback, G. Wieslander, W. Nystad, M. Canciani, P. Sestini, G. Viegi, School air quality related to dry cough, rhinitis and nasal patency in children, Eur. Respir. J. 35 (2010) 742–749. https://doi.org/10.1183/09031936.00016309.

[6] M.K. Kim, J.-H. Choi, Can increased outdoor CO_2 concentrations impact on the ventilation and energy in buildings? A case study in Shanghai, China, Atmos. Environ. 210 (2019) 220–230. https://doi.org/10.1016/j.atmosenv.2019.04.015.

[7] J.A. Gonzalez, S. Algaba, C. Andrade, Corrosion of reinforcing bars in carbonated concrete, Br. Corros. J. 15 (1980) 135–139. https://doi.org/10.1179/bcj.1980.15.3.135.

[8] A. Steffens, D. Dinkler, H. Ahrens, Modeling carbonation for corrosion risk prediction of concrete structures, Cem. Concr. Res. 32 (2002) 935–941. https://doi.org/10.1016/S0008-8846(02)00728-7.

[9] U. Angst, B. Elsener, A. Jamali, B. Adey, Concrete cover cracking owing to reinforcement corrosion - theoretical considerations and practical experience: Concrete cover cracking owing to reinforcement corrosion, Mater. Corros. 63 (2012) 1069–1077. https://doi.org/10.1002/maco.201206669.

[10] V.G. Papadakis, C.G. Vayenas, M.N. Fardis, A reaction engineering approach to the problem of concrete carbonation, AIChE J. 35 (1989) 1639–1650. https://doi.org/10.1002/aic.690351008.

[11] B. Lagerblad, Carbon dioxide uptake during concrete life cycle – State of the art, Stockholm: Swedish Cement and Concrete Research Institute (2005).
[12] C. Pade, M. Guimaraes, The CO_2 uptake of concrete in a 100 year perspective, Cem. Concr. Res. 37 (2007) 1348–1356. https://doi.org/10.1016/j.cemconres.2007.06.009.
[13] Z. Cao, R.J. Myers, R.C. Lupton, H. Duan, R. Sacchi, N. Zhou, T. Reed Miller, J.M. Cullen, Q. Ge, G. Liu, The sponge effect and carbon emission mitigation potentials of the global cement cycle, Nat. Commun. 11 (2020) 3777. https://doi.org/10.1038/s41467-020-17583-w.
[14] J. Sercombe, R. Vidal, C. Gallé, F. Adenot, Experimental study of gas diffusion in cement paste, Cem. Concr. Res. 37 (2007) 579–588. https://doi.org/10.1016/j.cemconres.2006.12.003.
[15] Y. Houst, The role of moisture in the carbonation of cementitious materials, Restor. Build. Monum. 2 (1996) 49–66. https://doi.org/10.1515/rbm-1996-5083.
[16] B. Bary, A. Sellier, Coupled moisture—carbon dioxide–calcium transfer model for carbonation of concrete, Cem. Concr. Res. 34 (2004) 1859–1872. https://doi.org/10.1016/j.cemconres.2004.01.025.
[17] A. Morandeau, M. Thiéry, P. Dangla, Investigation of the carbonation mechanism of CH and C-S-H in terms of kinetics, microstructure changes and moisture properties, Cem. Concr. Res. 56 (2014) 153–170. https://doi.org/10.1016/j.cemconres.2013.11.015.
[18] J. Jeong, A.S. Alemu, S. Park, H.K. Lee, G. Liyew, H. Ramézani, V.G. Papadakis, H.-K. Kim, Phase profiling of carbonated cement paste: Quantitative X-ray diffraction analysis and numerical modeling, Case Stud. Constr. Mater. 16 (2022) e00890. https://doi.org/10.1016/j.cscm.2022.e00890.
[19] V. Shah, K. Scrivener, B. Bhattacharjee, S. Bishnoi, Changes in microstructure characteristics of cement paste on carbonation, Cem. Concr. Res. 109 (2018) 184–197. https://doi.org/10.1016/j.cemconres.2018.04.016.
[20] H. Cui, W. Tang, W. Liu, Z. Dong, F. Xing, Experimental study on effects of CO_2 concentrations on concrete carbonation and diffusion mechanisms, Constr. Build. Mater. 93 (2015) 522–527. https://doi.org/10.1016/j.conbuildmat.2015.06.007.
[21] J. Sang-Hwa, L. Myung-Kue, K. Jee-Sang, Experimental Study on CO_2 Diffusivity in Cementitious Materials, Corros. Sci. Technol. 4 (2005) 69–74.
[22] J.M. Torrenti, O. Amiri, L. Barnes-Davin, F. Bougrain, S. Braymand, B. Cazacliu, J. Colin, A. Cudeville, P. Dangla, A. Djerbi, M. Doutreleau, A. Feraille, M. Gueguen, X. Guillot, Y. Hou, L. Izoret, Y.-P. Jacob, J. Jeong, J.D.L. Hiu Hoong, P.-Y. Mahieux, J. Mai-Nhu, H. Martinez, V. Meyer, V. Morin, T. Pernin, J.-M. Potier, L. Poulizac, P. Rougeau, M. Saadé, L. Schmitt, T. Sedran, M. Sereng, A. Soive, G.S. Dos Reys, P. Turcry, The FastCarb project: Taking advantage of the accelerated carbonation of recycled concrete aggregates, Case Stud. Constr. Mater. 17 (2022) e01349. https://doi.org/10.1016/j.cscm.2022.e01349.
[23] B. Lu, C. Shi, Z. Cao, M. Guo, J. Zheng, Effect of carbonated coarse recycled concrete aggregate on the properties and microstructure of recycled concrete, J. Cleaner Prod. 233 (2019) 421–428. https://doi.org/10.1016/j.jclepro.2019.05.350.
[24] C.O. Ania, E. Raymundo-Piñero, Nanoporous Carbons with Tuned Porosity, in: K. Kaneko, F. Rodríguez-Reinoso (Eds.), Nanoporous Materials for Gas Storage, Springer, Singapore, 2019: pp. 91–135. https://doi.org/10.1007/978-981-13-3504-4_5.
[25] R.C. Bansal, M. Goyal, Adsorption Energetics, Models and Isotherm Equation, in: Activated Carbon Adsorption, Taylor & Francis, 2005: pp. 67–143. https://doi.org/10.1201/9781420028812.

[26] B. Akash, W. O'Brien, The production of activated carbon from a bituminous coal, Int. J. Energy Res. 20 (1996) 913–922. https://doi.org/10.1002/(SICI)1099-114X(199610)20:10<913::AID-ER205>3.0.CO;2-7.
[27] O. Duggan, S.J. Allen, Study of the physical and chemical characteristics of a range of chemically treated, lignite based carbons, Water Sci. Technol. 35 (1997) 21–27. https://doi.org/10.1016/S0273-1223(97)00110-8.
[28] G. Singh, K.S. Lakhi, S. Sil, S.V. Bhosale, I. Kim, K. Albahily, A. Vinu, Biomass derived porous carbon for CO_2 capture, Carbon 148 (2019) 164–186. https://doi.org/10.1016/j.carbon.2019.03.050.
[29] D. Woolf, J.E. Amonette, F.A. Street-Perrott, J. Lehmann, S. Joseph, Sustainable biochar to mitigate global climate change, Nat. Commun. 1 (2010) 56. https://doi.org/10.1038/ncomms1053.
[30] R. Renner, Rethinking biochar, Environ. Sci. Technol. (2007) 5932–5933.
[31] P.D. Dissanayake, S. You, A.D. Igalavithana, Y. Xia, A. Bhatnagar, S. Gupta, H.W. Kua, S. Kim, J.-H. Kwon, D.C.W. Tsang, Y.S. Ok, Biochar-based adsorbents for carbon dioxide capture: A critical review, Renew. Sustain. Energy Rev. 119 (2020) 109582. https://doi.org/10.1016/j.rser.2019.109582.
[32] S.S. Senadheera, S. Gupta, H.W. Kua, D. Hou, S. Kim, D.C.W. Tsang, Y.S. Ok, Application of biochar in concrete – A review, Cem. Concr. Compos. 143 (2023) 105204. https://doi.org/10.1016/j.cemconcomp.2023.105204.
[33] S. Praneeth, R. Guo, T. Wang, B.K. Dubey, A.K. Sarmah, Accelerated carbonation of biochar reinforced cement-fly ash composites: Enhancing and sequestering CO_2 in building materials, Constr. Build. Mater. 244 (2020) 118363. https://doi.org/10.1016/j.conbuildmat.2020.118363.
[34] S. Gupta, S. Muthukrishnan, H.W. Kua, Comparing influence of inert biochar and silica rich biochar on cement mortar – Hydration kinetics and durability under chloride and sulfate environment, Constr. Build. Mater. 268 (2021) 121142. https://doi.org/10.1016/j.conbuildmat.2020.121142.
[35] S. Gupta, H.W. Kua, C.Y. Low, Use of biochar as carbon sequestering additive in cement mortar, Cem. Concr. Compos. 87 (2018) 110–129. https://doi.org/10.1016/j.cemconcomp.2017.12.009.
[36] X. Yang, X.-Y. Wang, Strength and durability improvements of biochar-blended mortar or paste using accelerated carbonation curing, J. CO_2 Util. 54 (2021) 101766. https://doi.org/10.1016/j.jcou.2021.101766.
[37] T. Chen, L. Zhao, X. Gao, L. Li, L. Qin, Modification of carbonation-cured cement mortar using biochar and its environmental evaluation, Cem. Concr. Compos. 134 (2022) 104764. https://doi.org/10.1016/j.cemconcomp.2022.104764.
[38] P.F.E. Gunn, C.C. Onn, K.H. Mo, H.V. Lee, Enhancing carbon sequestration in cement mortar using high volume local rice husk biochar coupled with carbonation curing, Case Stud. Constr. Mater. 21 (2024) e03591. https://doi.org/10.1016/j.cscm.2024.e03591.
[39] H.W. Kua, Biochar as building and road materials, in: Biochar for Environmental Management: Science, Technology and Implementation, 3rd ed., Routledge, London, 2024. https://doi.org/10.4324/9781003297673.
[40] H.W. Kua, S.M.H. Tan, Novel typology of accelerated carbonation curing: using dry and pre-soaked biochar to tune carbon capture and mechanical properties of cementitious mortar, Biochar 5 (2023) 36. https://doi.org/10.1007/s42773-023-00234-w.
[41] S. Gupta, H.W. Kua, S.D. Pang, Effect of biochar on mechanical and permeability properties of concrete exposed to elevated temperature, Constr. Build. Mater. 234 (2020) 117338. https://doi.org/10.1016/j.conbuildmat.2019.117338.

[42] M. Horgnies, I. Dubois-Brugger, N.J. Krou, I. Batonneau-Gener, T. Belin, S. Mignard, Reactivity of NO_2 and CO_2 with hardened cement paste containing activated carbon, Eur. Phys. J. Spec. Top. 224 (2015) 1985–1994. https://doi.org/10.1140/epjst/e2015-02515-7.
[43] M. Horgnies, I. Dubois-Brugger, E.M. Gartner, NOx de-pollution by hardened concrete and the influence of activated charcoal additions, Cem. Concr. Res. 42 (2012) 1348–1355. https://doi.org/10.1016/j.cemconres.2012.06.007.
[44] M. Horgnies, F. Serre, I. Dubois-Brugger, E. Gartner, NOx De-pollution using activated charcoal concrete—From laboratory experiments to tests with prototype garages, Cem. Concr. Res. 42 (2014) 1348–1355.
[45] E. Raymundo-Piñero, M. Cadek, F. Béguin, Tuning Carbon Materials for Supercapacitors by Direct Pyrolysis of Seaweeds, Adv. Funct. Mater. 19 (2009) 1032–1039. https://doi.org/10.1002/adfm.200801057.
[46] E. Raymundo-Piñero, M. Cadek, M. Wachtler, F. Béguin, Carbon Nanotubes as Nanotexturing Agents for High Power Supercapacitors Based on Seaweed Carbons, ChemSusChem 4 (2011) 943–949. https://doi.org/10.1002/cssc.201000376.
[47] H. Giesche, Mercury Porosimetry: A General (Practical) Overview, Part. Part. Syst. Charact. 23 (2006) 9–19. https://doi.org/10.1002/ppsc.200601009.
[48] A. Rita Damasceno Costa, J. Pereira Gonçalves, Accelerated carbonation of ternary cements containing waste materials, Constr. Build. Mater. 302 (2021) 124159. https://doi.org/10.1016/j.conbuildmat.2021.124159.
[49] D. Frenkel, B. Smit, Monte Carlo Simulations, in: Understanding Molecular Simulation: From Algorithms to Applications, Academic Press San Diego, 2002: pp. 23–65. https://doi.org/10.1063/1.881812.
[50] M.P. Allen, D.J. Tildesley, Monte Carlo Methods, in: Computer Simulation of Liquids, Oxford university press, 2017: pp. 147–184. https://doi.org/10.1093/oso/9780198803195.001.0001.
[51] T.X. Nguyen, S.K. Bhatia, Characterization of accessible and inaccessible pores in microporous carbons by a combination of adsorption and small angle neutron scattering, Carbon 50 (2012) 3045–3054. https://doi.org/10.1016/j.carbon.2012.02.091.
[52] G. Opletal, T.C. Petersen, S.P. Russo, HRMC_2. 1: Hybrid Reverse Monte Carlo method with silicon, carbon, germanium and silicon carbide potentials, Comput. Phys. Commun. 185 (2014) 1854–1855. https://doi.org/10.1016/j.cpc.2014.02.025.
[53] G. Opletal, T. Petersen, B. O'Malley, I. Snook, D.G. McCulloch, N.A. Marks, I. Yarovsky, Hybrid approach for generating realistic amorphous carbon structure using metropolis and reverse Monte Carlo, Mol. Simul. 28 (2002) 927–938. https://doi.org/10.1080/0892702040000025584.
[54] Z. El Oufir, H. Ramezani, N. Mathieu, S. Delpeux, Impact of adsorbent carbons and carbon surface conductivity on adsorption capacity of CO_2, CH_4, N_2 and gas separation, Comput. Mater. Sci. 199 (2021) 110572. https://doi.org/10.1016/j.commatsci.2021.110572.
[55] Z. El Oufir, H. Ramézani, N. Mathieu, S. Delpeux, S.K. Bhatia, Influence of force field used in carbon nanostructure reconstruction on simulated phenol adsorption isotherms in aqueous medium, J. Mol. Liq. 344 (2021) 117548. https://doi.org/10.1016/j.molliq.2021.117548.
[56] A.H. Farmahini, S.K. Bhatia, Hybrid Reverse Monte Carlo simulation of amorphous carbon: Distinguishing between competing structures obtained using different modeling protocols, Carbon 83 (2015) 53–70. https://doi.org/10.1016/j.carbon.2014.11.013.

[57] H. Ramézani, J. Jeong, S.K. Bhatia, V.G. Papadakis, Assessment of CO_2 adsorption capacity in Wollastonite using atomistic simulation, J. CO_2 Util. 50 (2021) 101564. https://doi.org/10.1016/j.jcou.2021.101564.
[58] M.P. Bichat, E. Raymundo-Piñero, F. Béguin, High voltage supercapacitor built with seaweed carbons in neutral aqueous electrolyte, Carbon 48 (2010) 4351–4361. https://doi.org/10.1016/j.carbon.2010.07.049.
[59] H. Marsh, F. Rodríguez-Reinoso, Characterization of Activated Carbon, in: Activated Carbon, 1st ed, Elsevier, Amsterdam Boston, 2006: pp. 143–242. https://doi.org/10.1016/B978-0-08-044463-5.X5013-4.
[60] A.A. Hilal, Microstructure of Concrete, in: S. Yilmaz, H.B. Ozmen (Eds.), High Performance Concrete Technology and Applications, InTech, Rijeka, 2016: pp. 3–24. https://doi.org/10.5772/64574.
[61] K. Aligizaki, Introduction, in: Pore Structure of Cement-Based Materials: Testing, Interpretation and Requirements, Taylor & Francis, Abingdon, 2006: pp. 1–32. https://doi.org/10.1201/9781482271959.
[62] M.G. Richardson, Permeability and transport processes, in: Fundamentals of Durable Reinforced Concrete, Spon Press, London; New York, 2002: pp. 38–50. https://doi.org/10.1201/9781482272109.
[63] K.L. Scrivener, A.K. Crumbie, P. Laugesen, The interfacial transition zone (ITZ) between cement paste and aggregate in concrete, Interface Sci. 12 (2004) 411–421. https://doi.org/10.1023/B:INTS.0000042339.92990.4c.
[64] R. Zimbelmann, A method for strengthening the bond between cement stone and aggregates, Cem. Concr. Res. 17 (1987) 651–660. https://doi.org/10.1016/0008-8846(87)90138-4.
[65] J. Ollivier, J. Maso, B. Bourdette, Interfacial transition zone in concrete, Adv. Cem. Based Mater. 2 (1995) 30–38. https://doi.org/10.1016/1065-7355(95)90037-3.
[66] A. Elsharief, M.D. Cohen, J. Olek, Influence of aggregate size, water cement ratio and age on the microstructure of the interfacial transition zone, Cem. Concr. Res. 33 (2003) 1837–1849. https://doi.org/10.1016/S0008-8846(03)00205-9.
[67] J. Zhang, C. Shi, Y. Li, X. Pan, C.-S. Poon, Z. Xie, Performance Enhancement of Recycled Concrete Aggregates through Carbonation, J. Mater. Civ. Eng. 27 (2015) 04015029. https://doi.org/10.1061/(ASCE)MT.1943-5533.0001296.
[68] S. Gupta, H.W. Kua, Effect of water entrainment by pre-soaked biochar particles on strength and permeability of cement mortar, Constr. Build. Mater. 159 (2018) 107–125. https://doi.org/10.1016/j.conbuildmat.2017.10.095.
[69] A. Sirico, P. Bernardi, B. Belletti, A. Malcevschi, E. Dalcanale, I. Domenichelli, P. Fornoni, E. Moretti, Mechanical characterization of cement-based materials containing biochar from gasification, Constr. Build. Mater. 246 (2020) 118490. https://doi.org/10.1016/j.conbuildmat.2020.118490.
[70] T. Nishikawa, K. Suzuki, Chemical conversion of C-S-H in concrete, Cem. Concr. Res. 24 (1994) 176–182. https://doi.org/10.1016/0008-8846(94)90099-X.
[71] T. Nishikawa, K. Suzuki, S. Ito, K. Sato, T. Takebe, Decomposition of synthesized ettringite by carbonation, Cem. Concr. Res. 22 (1992) 6–14. https://doi.org/10.1016/0008-8846(92)90130-N.
[72] N. Vogler, P. Drabetzki, M. Lindemann, H.-C. Kühne, Description of the concrete carbonation process with adjusted depth-resolved thermogravimetric analysis, J. Therm. Anal. Calorim. 147 (2022) 6167–6180. https://doi.org/10.1007/s10973-021-10966-1.
[73] D. Torréns-Martín, L. Fernández-Carrasco, M.T. Blanco-Varela, Thermal analysis of blended cements, J. Therm. Anal. Calorim. 121 (2015) 1197–1204. https://doi.org/10.1007/s10973-015-4569-1.

[74] M. Thiery, G. Villain, P. Dangla, G. Platret, Investigation of the carbonation front shape on cementitious materials: Effects of the chemical kinetics, Cem. Concr. Res. 37 (2007) 1047–1058. https://doi.org/10.1016/j.cemconres.2007.04.002.
[75] C. Liu, Z. Liu, Y. Zhang, A multi-scale framework for modelling effective gas diffusivity in dry cement paste: Combined effects of surface, Knudsen and molecular diffusion, Cem. Concr. Res. 131 (2020) 106035. https://doi.org/10.1016/j.cemconres.2020.106035.
[76] Y.F. Houst, F.H. Wittmann, Influence of porosity and water content on the diffusivity of CO_2 and O_2 through hydrated cement paste, Cem. Concr. Res. 24 (1994) 1165–1176.
[77] J.J. Chen, J.J. Thomas, H.M. Jennings, Decalcification shrinkage of cement paste, Cem. Concr. Res. 36 (2006) 801–809. https://doi.org/10.1016/j.cemconres.2005.11.003.
[78] K.-H. Yang, E.-A. Seo, S.-H. Tae, Carbonation and CO_2 uptake of concrete, Environ. Impact Assess. Rev. 46 (2014) 43–52. https://doi.org/10.1016/j.eiar.2014.01.004.
[79] S. Steiner, T. Proske, F. Winnefeld, B. Lothenbach, Effect of limestone fillers on CO2 and water vapour diffusion in carbonated concrete, Cement 8 (2022) 100027. https://doi.org/10.1016/j.cement.2022.100027.
[80] M. Jebli, F. Jamin, E. Malachanne, E. Garcia-Diaz, M.S. El Youssoufi, Experimental characterization of mechanical properties of the cement-aggregate interface in concrete, Constr. Build. Mater. 161 (2018) 16–25. https://doi.org/10.1016/j.conbuildmat.2017.11.100.
[81] R.A. Berner, A.C. Lasaga, R.M. Garrels, Carbonate-silicate geochemical cycle and its effect on atmospheric carbon dioxide over the past 100 million years, Am. J. Sci. 283 (1983) 641–683. https://doi.org/10.2475/ajs.283.7.641.
[82] W. Dreybrodt, J. Lauckner, L. Zaihua, U. Svensson, D. Buhmann, The kinetics of the reaction $CO_2 + H_2O \rightarrow H^+ + HCO_3^-$ as one of the rate limiting steps for the dissolution of calcite in the system H_2O-CO_2-$CaCO_3$, Geochim. Cosmochim. Acta 60 (1996) 3375–3381. https://doi.org/10.1016/0016-7037(96)00181-0.
[83] G.H. Rau, K. Caldeira, Enhanced carbonate dissolution: a means of sequestering waste CO2 as ocean bicarbonate, Energy Convers. Manag. 40 (1999) 1803–1813.
[84] G.H. Rau, CO_2 mitigation via capture and chemical conversion in seawater, Environ. Sci. Technol. 45 (2011) 1088–1092. https://doi.org/10.1021/es102671x.
[85] M. Samari, F. Ridha, V. Manovic, A. Macchi, E.J. Anthony, Direct capture of carbon dioxide from air via lime-based sorbents, Mitig. Adapt. Strateg. Glob. Chang. 25 (2020) 25–41. https://doi.org/10.1007/s11027-019-9845-0.
[86] Z. Liu, W. Dreybrodt, Significance of the carbon sink produced by H_2O–carbonate–CO_2–aquatic phototroph interaction on land, Sci. Bull. 60 (2015) 182–191. https://doi.org/10.1007/s11434-014-0682-y.
[87] F. Pontiga, J.M. Valverde, H. Moreno, F.J. Duran-Olivencia, Dry gas–solid carbonation in fluidized beds of $Ca(OH)_2$ and nanosilica/$Ca(OH)_2$ at ambient temperature and low CO2 pressure, Chem. Eng. J. 222 (2013) 546–552. https://doi.org/10.1016/j.cej.2013.02.067.

Tables

Table 1 : Formulations for Type I and Type II composite materials expressed in g.cm^{-3}

Composition (g.cm^{-3})	Type I	Type II
CEM I 52.5	0.508	0.509
RCA	0.623	0.406
Porous carbon	-	0.013
Effective water	0.201	0.201
w/c[a]	0.45	0.45
a/c[b]	1.22	0.79

[a]water/cement weight ratio

[b]agregate(+carbon)/cement weight ratio

Table 2 : Mercury Intrusion porosimetry (MIP) and hydro-static weighing (HW) results obtained on LN750, RCA and Type I and Type II composite materials after hydration: Open porosity Φ, bulk density ρ_b, skeletal density ρ_s, average pore diameter and water sorption (WA)

		LN 750	RCA	Type I - NC	Type II - NC
MIP	Φ (%) 0.006<d<0.3 µm	-	7.0 ± 1.6	9.5 ± 0.6	14.9 ± 0.2
	Φ (%) 0.3<d<4 µm	35.9 ± 0.7	4.0 ± 0.9	1.8 ± 0.2	10.2 ± 1.1
	Φtot (%)	49.2 ± 0.1	16.4 ± 2.2	13.3 ± 0.2	30.5 ± 1.3
	ρ_b (g.cm^{-3})	0.15 ± 0.00	2.01 ± 0.04	1.96 ± 0.02	1.56 ± 0.03
HW	Φtot (%)	92.6 ± 0.6	10.9 ± 0.6	18.2 ± 1.1	35.5 ± 1.1
	ρ_b (g.cm^{-3})	0.12 ± 0.01	2.41 ± 0.02	2.15 ± 0.05	1.65 ± 0.03
	ρ_s (g.cm^{-3})	1.69 ± 0.23	2.70 ± 0.02	2.63 ± 0.02	2.56 ± 0.01
	WA (%)	746 ± 38	4.5 ± 0.3	8.5 ± 0.7	21.5 ± 1.1

Table 3 : Mercury Intrusion porosimetry (MIP) over Type I and Type II composites after 30 accelerated carbonation days

	Φ (%)	Φ (%)	Φtot	ρ_b
	0.006<d<0.3 µm	0.3<d<4 µm	%	g.cm^{-3}
Type I	8.2 ± 0.6	1.8 ± 0.0	12.0 ± 0.3	1.97 ± 0.01
Type II	11.1 ± 0.7	3.8 ± 0.7	17.7 ± 0.8	1.81 ± 0.09

Figure Captions

Figure 1: Composite materials preparation (a). Sections of the composite materials Type I (left) and Type II (right) after hydration (b).

Figure 2: Textural characterization. N_2 adsorption isotherm for LN750 at 77K (a) and NLDFT pore size distribution (b). MIP pore size distribution (c) and associated intruded volumes (d) for RCA, LN750 and composites Type I and Type II.

Figure 3: TPD-MS results combining weight losses and desorbed gas profiles obtained for Type I and Type II composites. Heating rate = 10 °C.min^{-1} under 100 ml.min^{-1} Ar flow.

Figure 4: Cross sections of the composite materials after different carbonation days, sprayed with phenolphthalein solution (pink areas correspond to non-carbonated material).

Figure 5: TPD-MS results combining weight losses and desorbed gas profiles obtained for Type I (a) and Type II (b) composites at different accelerated carbonation days. Heating rate = 10 °C.min^{-1} under 100 ml.min^{-1} Ar flow.

Figure 6: Detail on CO_2 evolution obtained for Type I and Type II composites at different accelerated carbonation days by TPD-MS (a). Quantification of the H_2O and CO_2 evolved from the thermal treatment of the composites at different carbonation days evolution in wt% of the total mass sample (b). CO_2 uptake given as gCO_2 evolved by cm² of the total accessible surface (c) and as gCO_2 evolved by cm^3 of the total sample volume (d).

Figure 7: Evolution of the pore size distribution obtained by MIP on Type I and II composites after 30 days of carbonation (a). Effect of 30 carbonation days on the capillary porosity percentage (b)

Figure 8: Fitting of the experimental CO_2 uptake in the Type I and Type II composites with the kinetic model (a). Scanned biochar particle (b) and numerical composite material (c). CO_2 concentration distribution on the cutting plane at 10 hours (d) and detail around biochar particle (e). Comparison of CO_2 concentration distribution through the sample thickness for a numerical material composed by a cement matrix and for a material composed by the cement matrix and a porous biochar particle at 1 sec, 10 sec and 10 hours (f).

Figure 9: Optical microscopy on biochar-cement interface over the initial Type II composite (a) and after 30 days of accelerated carbonation (b). TPD-MS results combining weight losses and desorbed CO_2 and H_2O gas profiles obtained for raw LN750 biochar (full lines) and on LN750 biochar extracted from a 30 days carbonated Type II composite (dashed lines) (c). Comparison of the desorbed CO_2 profiles after 30 carbonation days for the Type II composite and for the porous biochar extracted of that Type II composite.

Figure 10: (a) GCMC simulations performed at the interface between CSH and carbon (b) zooming images at the interface between CSH and carbon of separated adsorption of H_2O and CO_2.

Figure 11: Scheme of the dual carbonation mechanism occurring close to the biochar-cement interface. Grey dialog boxes correspond to initial carbonation since orange dialog boxes correspond to the additional $CaCO_3$ precipitation by weathering of calcite and further reaction with $Ca(OH)_2$ and CO_2 at the carbon/cement interface.

Figure 1

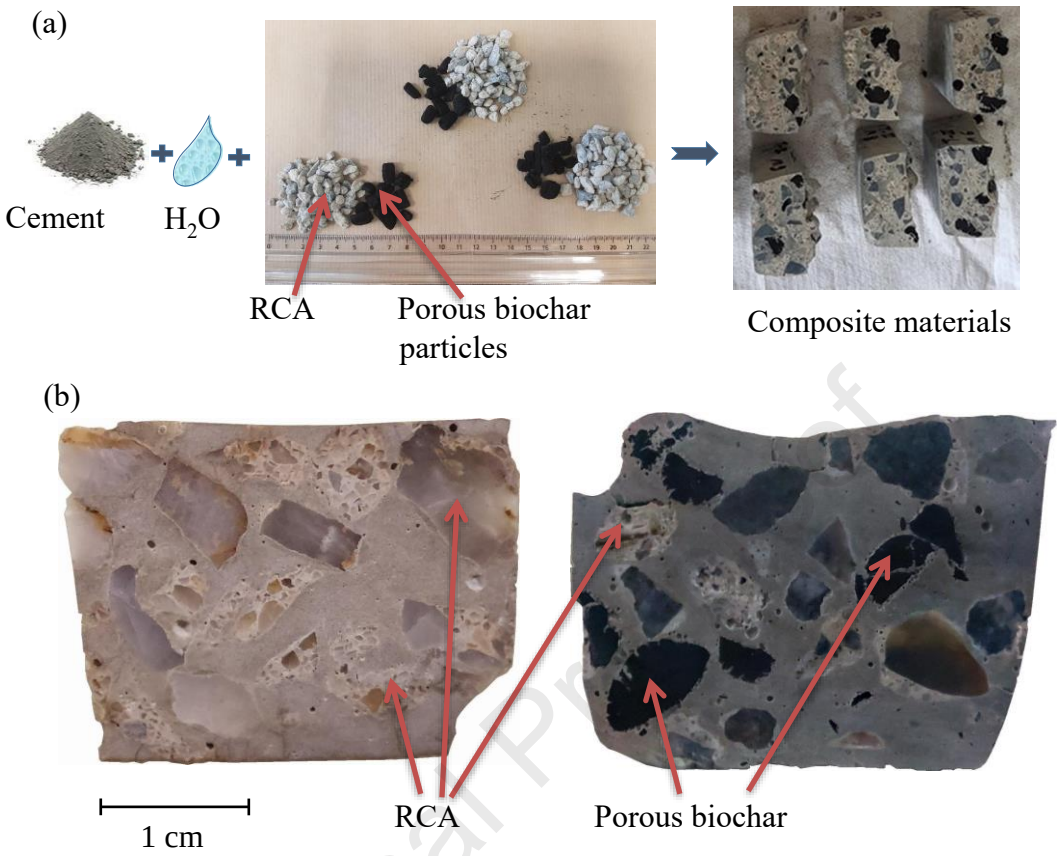

Figure 2

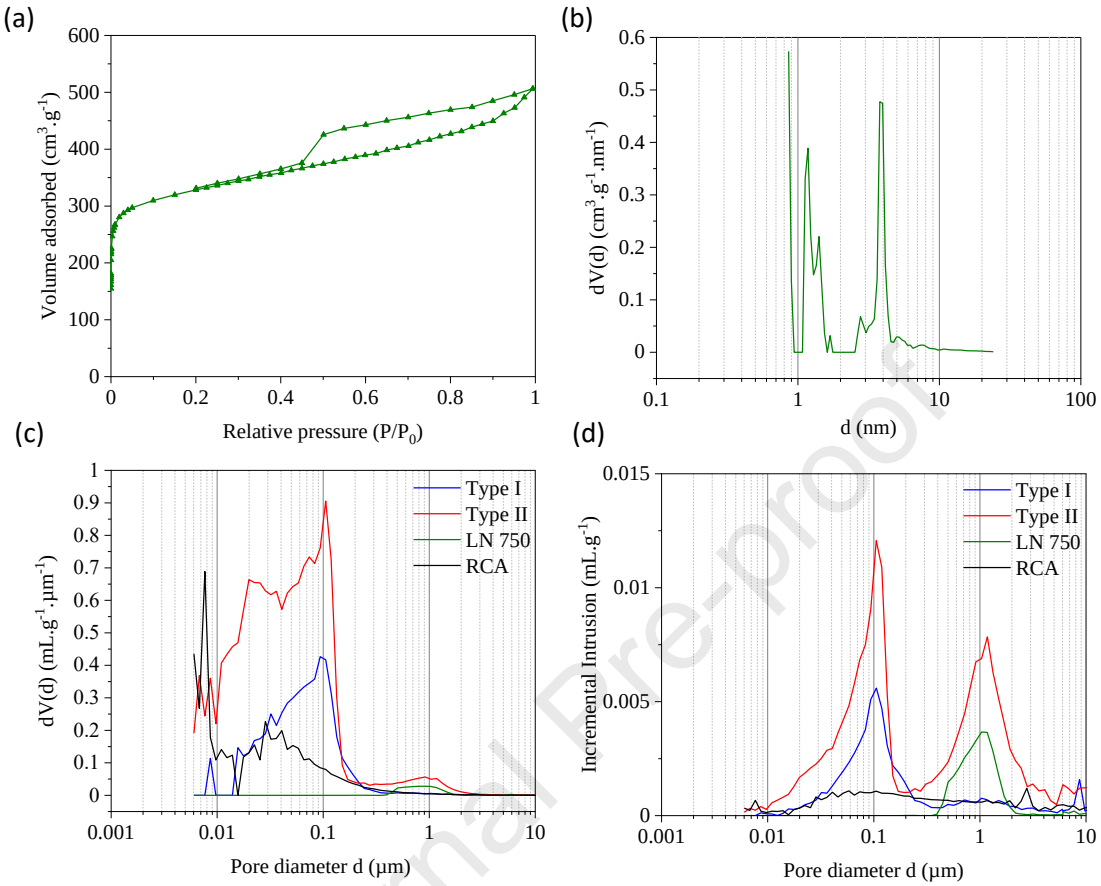

Figure 3

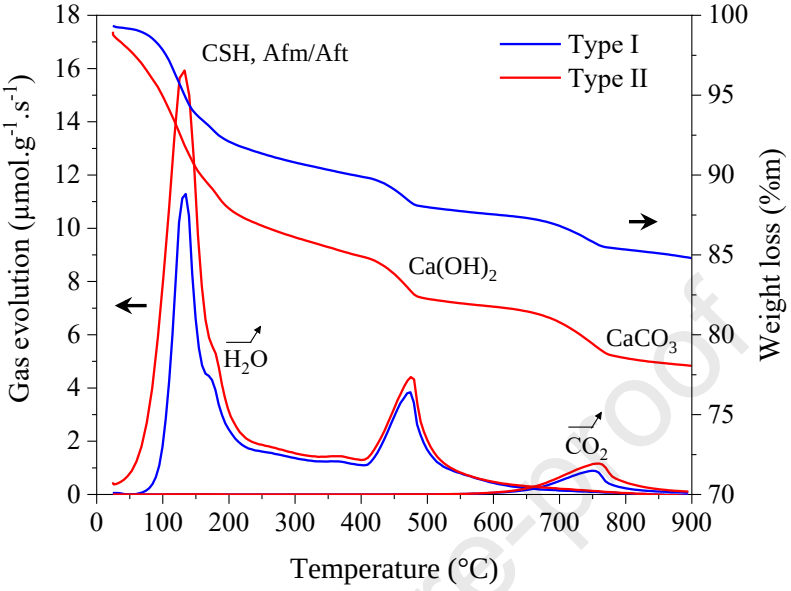

Figure 4

Figure 5

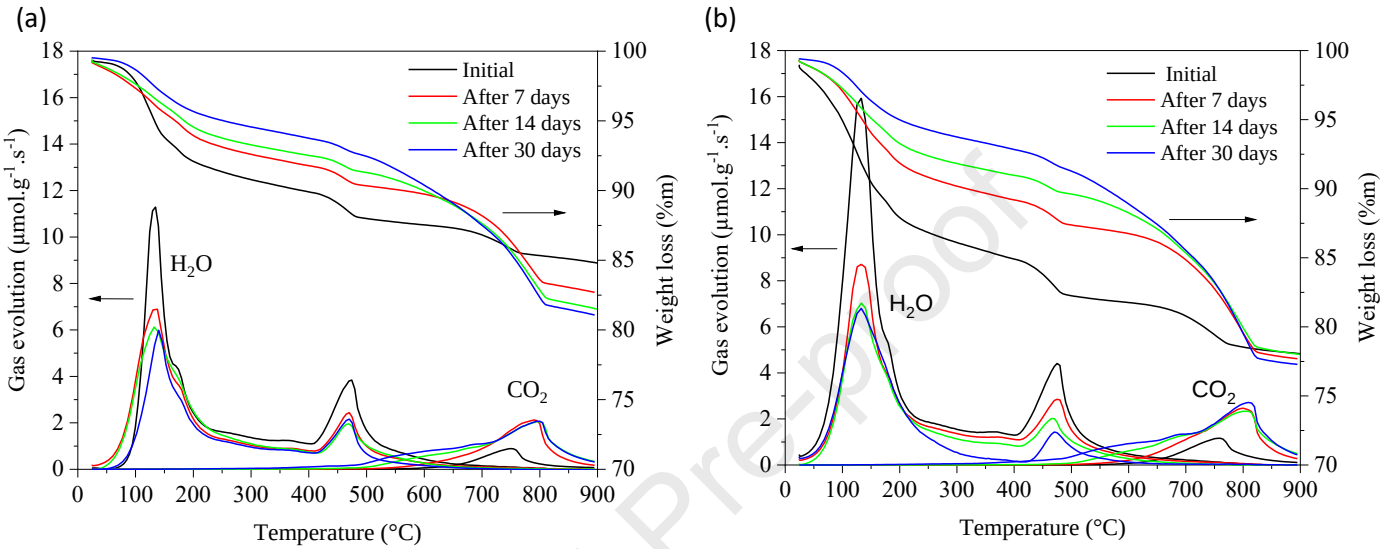

Figure 6

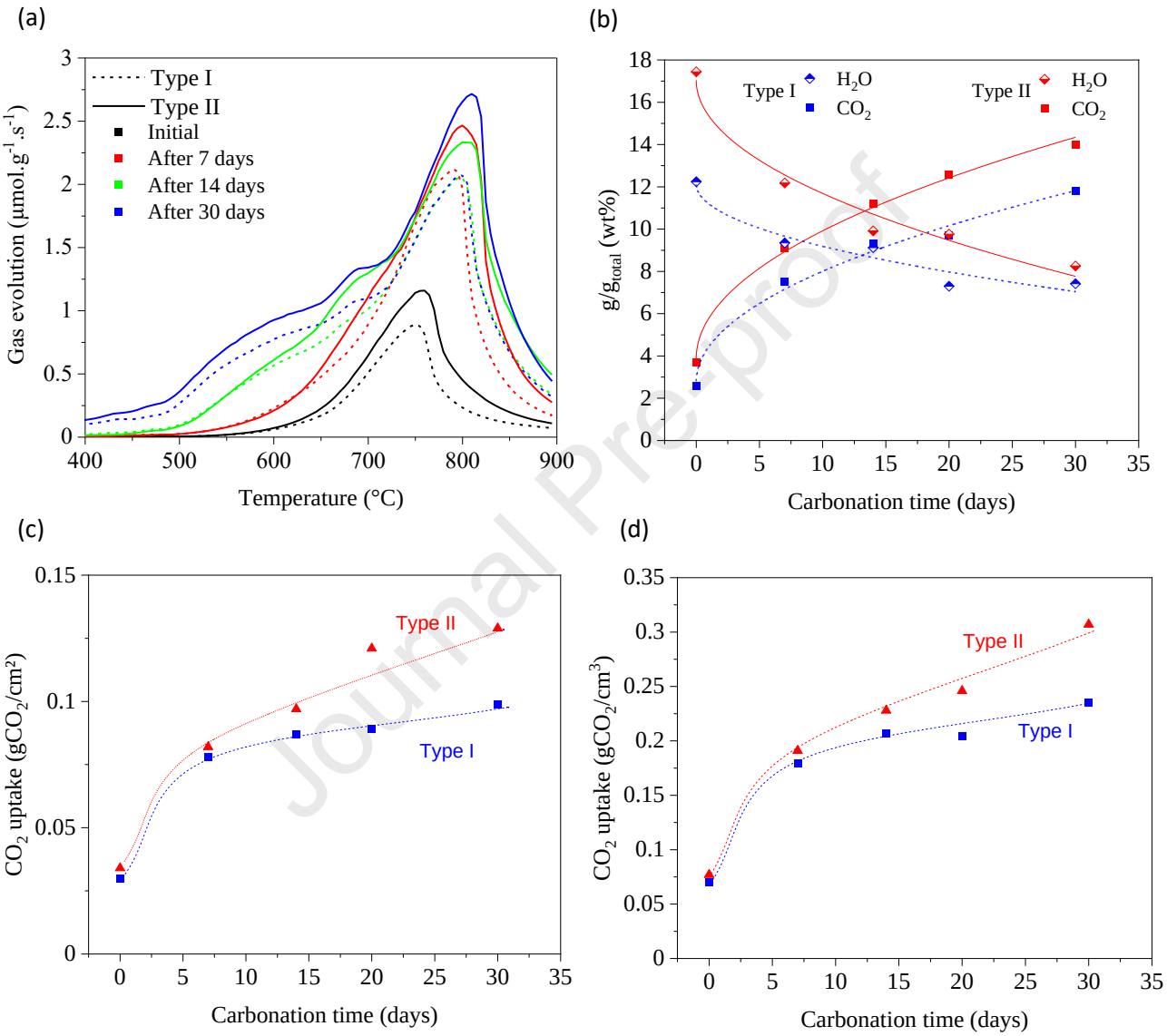

Figure 8

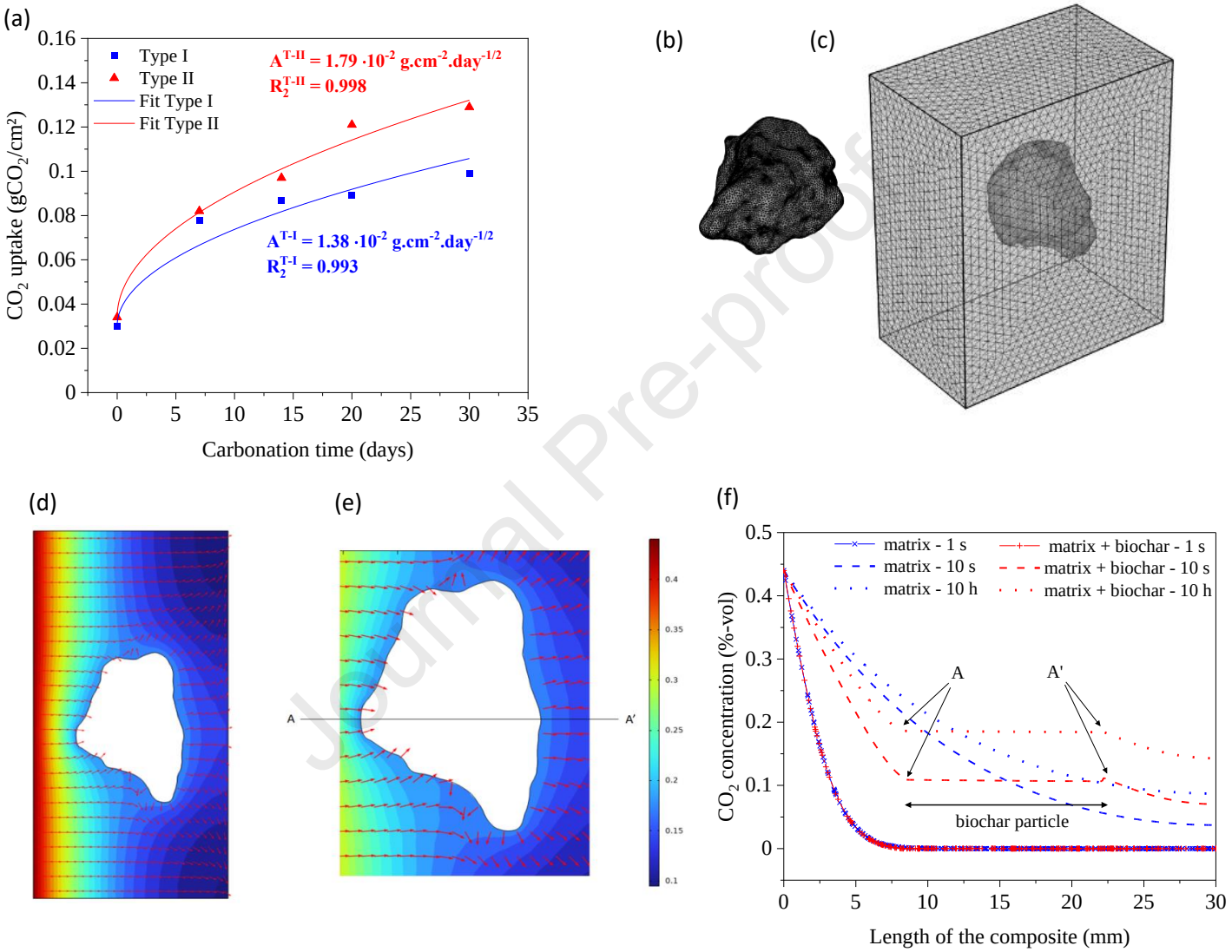

Figure 9

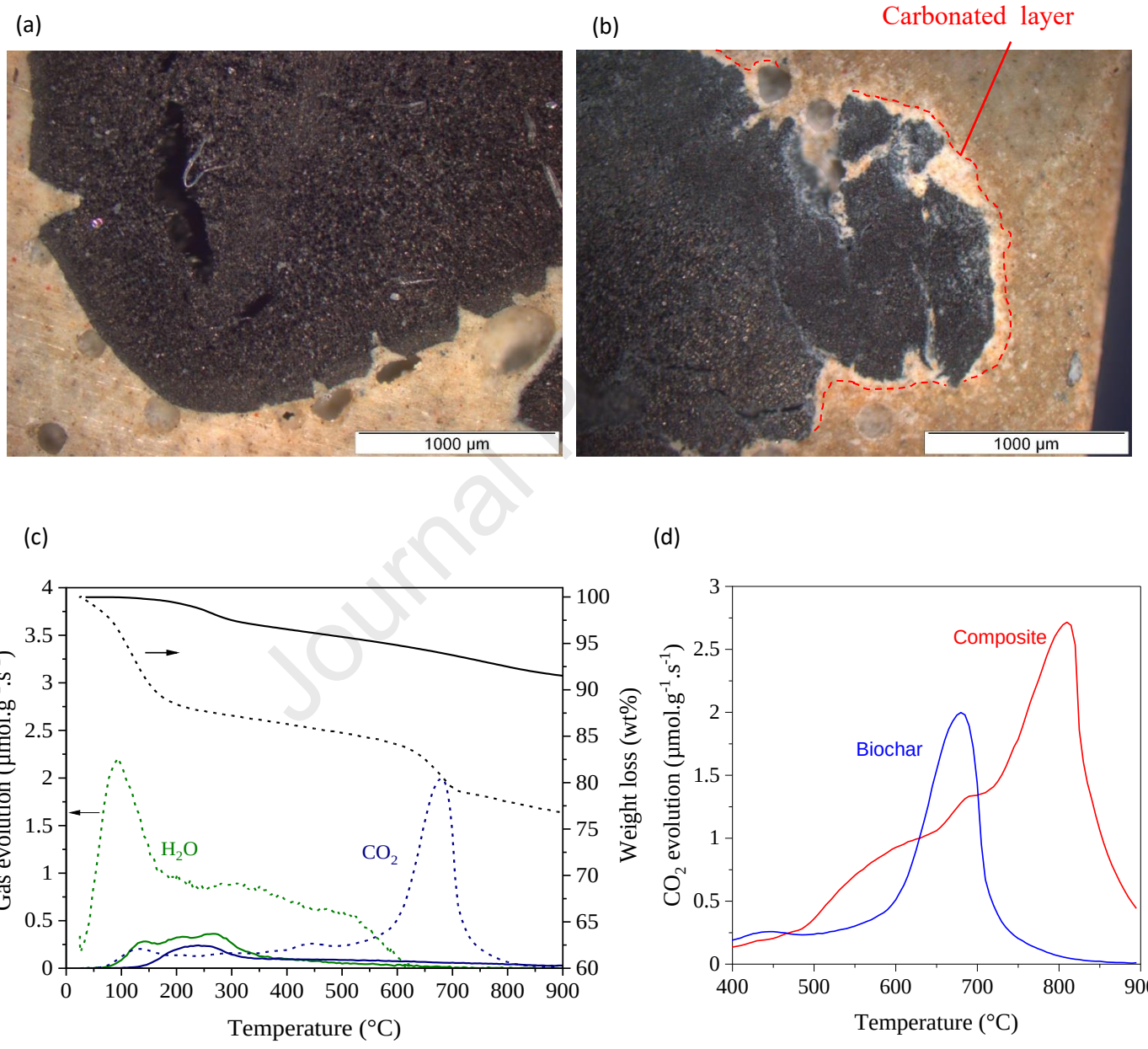

Figure 10

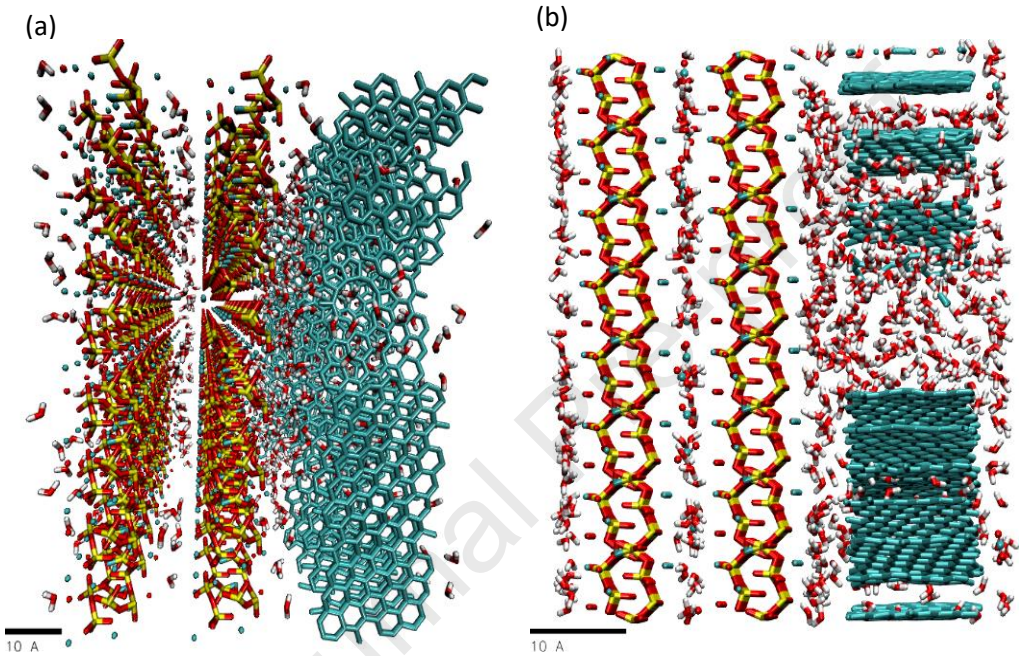

Figure 11

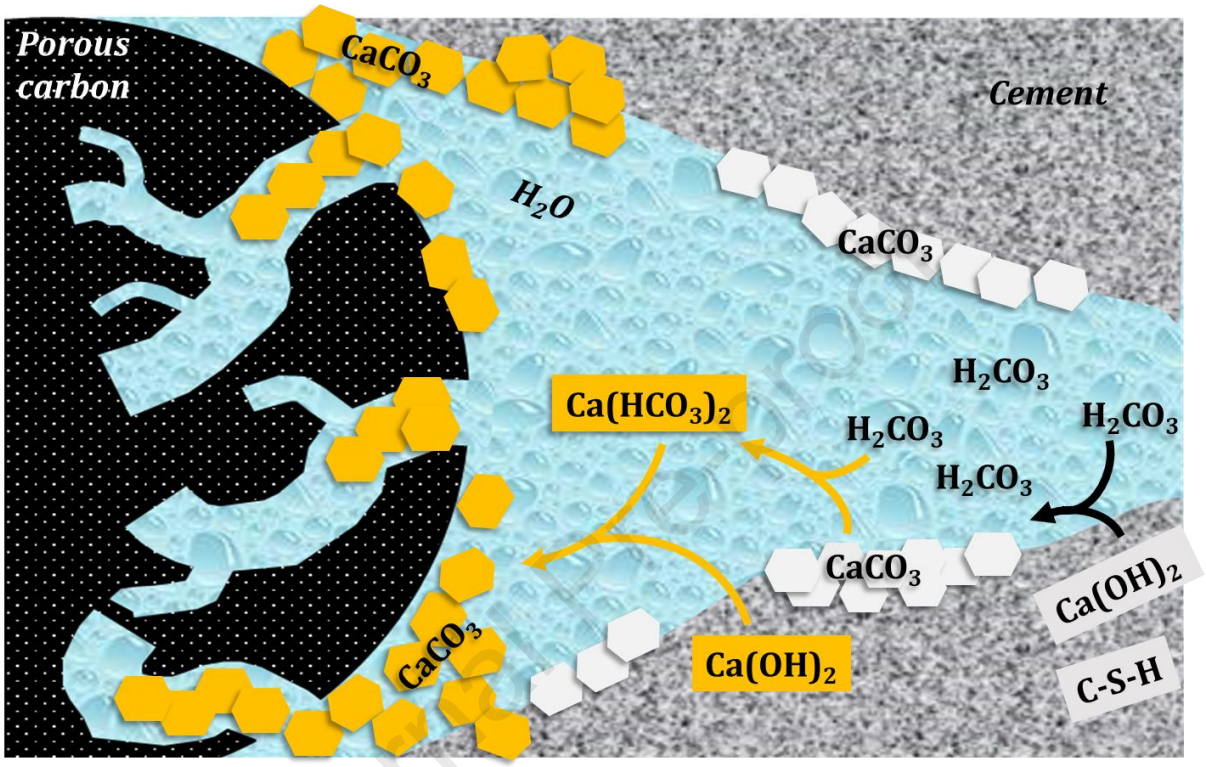

Figure 7

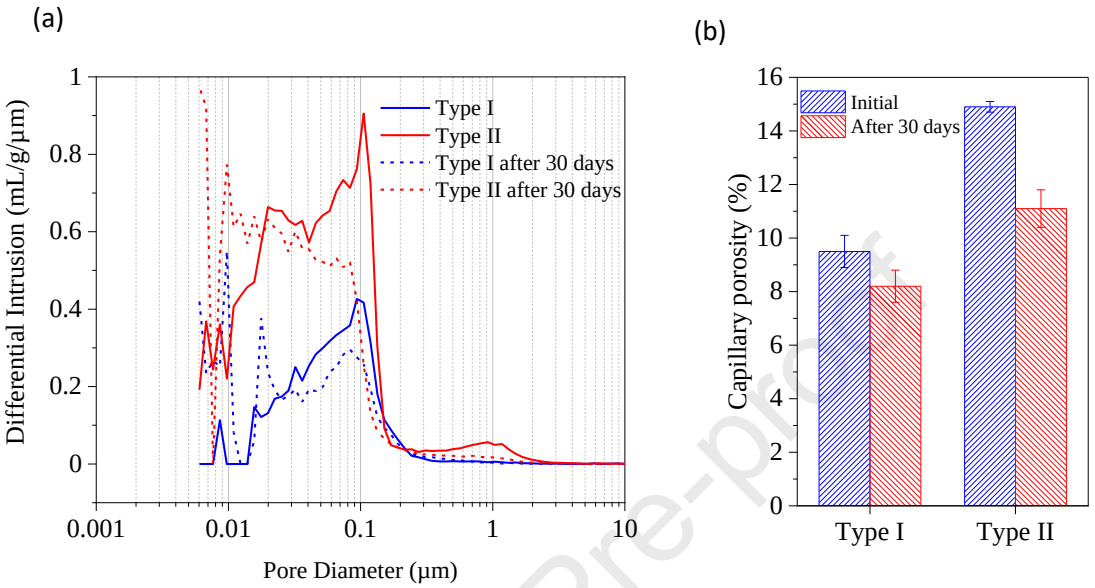

Highlights

- Porous biochar can overcome the slow carbonation kinetics of concrete
- Porous carbon allow increasing the conversion degree of carbonatable hydrates
- High local amount of water drives to an important development of capillary porosity
- Porous biochar increases the effective CO_2 diffusivity in the cement matrix
- Biochar participates in CO_2 uptake by physical and chemical mechanisms

Declaration of interests

☐ The authors declare that they have no known competing financial interests or personal relationships that could have appeared to influence the work reported in this paper.

☒ The authors declare the following financial interests/personal relationships which may be considered as potential competing interests:

Encarnacion Raymundo-Pinero reports financial support was provided by Centre-Val de Loire Region. Encarnacion Raymundo-Pinero has patent pending to Assignee. If there are other authors, they declare that they have no known competing financial interests or personal relationships that could have appeared to influence the work reported in this paper.